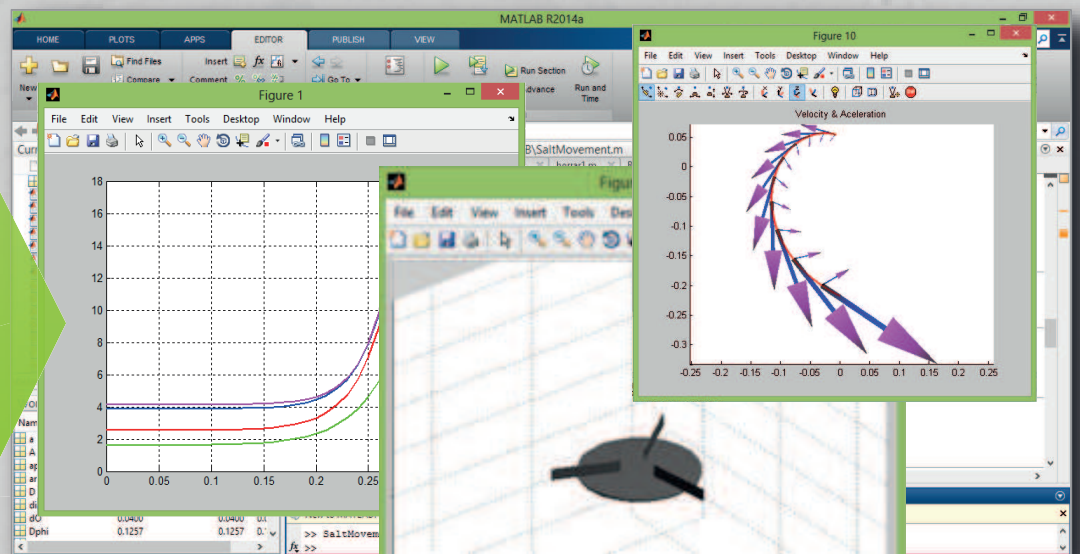


Mathematical modelling of the kinematics of a sub-cluster of salt particles in a spinning spreader disk

Paula Macías Vera
Master Final Dissertation





MSc in European Construction Engineering

Final dissertation defence: 19 September 2014

Mathematical modelling of the kinematics of a sub-cluster of salt particles in a spinning spreader disk

Author: Paula Macías Vera

Supervisors: Torben Brøchner

Regner Bæk Hessellund

Abstract

The kinematics of the flow of rock salt on a spreader disk is observed in full scale from movies recorded with a high speed camera and modelled by a novel kinematic shape function that includes a **radial scaling function** that can be successfully defined from three parameters. The motion of the particles in the close neighbourhood of the vane is modelled as a sub-cluster flow that implicitly incorporate the non-stationary flow complexities due to sliding, rolling and repositioning of the particles. The incremental prediction of the motion is based on the Newmark constant average acceleration method.

Keywords

spinning spreader disk, parameterise kinematics, image recognition, density estimation, time integration, radial scaling function

Research Statement

This final dissertation documents the work of a 20 ECTS MSc project under the auspices of the European study programme “Master in European Construction Engineering”.

The study has been carried out at the Engineering Centre Bygholm, Horsens, Aarhus University, under the supervision of Torben Brøchner, Associate Professor. The experimental part was performed in collaboration with the three Mechanical Engineering students, Peter Balogh, Csaba David Gyula and Fawad Mastour, as assistants.

Initially, a state of the art was elaborated and the research gap was specified.

In a first stage, time integration methods were investigated. The well-known Newmark Method was studied in further details and implemented algorithmically. This time integration method is an integral part of a novel approach for sub-cluster based kinematics that is currently under development (Brøchner & Macías, 2014). This method is based on the idea that complex kinematics can be parameterized and fitted to observations from high speed videos of real spreaders. In this MSc focus is on the fitting of observations to the model parameters. Therefore, real data was gathered from videos of full scale salt spreader in operation in a test plan for five different revolutions per minute. The experiments were performed at the facilities of and by equipment of the Engineering Centre Bygholm. The key finding of the study was that the novel model for radial kinematics could be defined to fit real world observations through a radial scaling function with only three parameters.

Acknowledgements

I would like to thank a couple of persons for their help and assistance during this master project. Big thanks to my main supervisor Torben Brøchner, Associate Professor, for giving me the opportunity to study such exciting topic, and for showing always confidence in me. Not a word of this dissertation could have been written without his inestimable support and guidance. I also like to thank my other supervisor Regner Bæk Hessellund, Senior Lecturer, who has always been willing to help. A special thanks to Krister Petterson, Director of the Engineering Centre Bygholm, who has received me in the institution with open arms, to the Mechanical Engineering students Fawad, Peter and Csaba patiently providing me the data needed for this work and to all staff in Bygholm in general for making me feel at home. Also a big thank to BREDAL A/S for letting me use their salt spreader for the many experiments.

Last but not least thanks to my wonderful partner Luis, my lovely family and my best friend María who have always supported me.

Notation

$t \in T_{AB} = [t_A, t_B]$	<i>time window</i>
Ω_{Ψ}	<i>sub-cluster</i>
Ψ	<i>generalized particle</i>
$\Omega: V_{\Omega}$	<i>subdomain, volume of a subdomain</i>
$\mathbf{x}_{xyz} = [x, y, z]_{\text{salt}}^T$	<i>instantaneous position vector in Cartesian coordinates</i>
$\dot{\mathbf{x}}_{xyz} = [\dot{x}, \dot{y}, \dot{z}]_{\text{salt}}^T$	<i>instantaneous velocity vector in Cartesian coordinates</i>
$\ddot{\mathbf{x}}_{xyz} = [\ddot{x}, \ddot{y}, \ddot{z}]_{\text{salt}}^T$	<i>instantaneous acceleration vector in Cartesian coordinates</i>
$\mathbf{x}_{r\theta z} = [\rho, \theta, z]_{\text{salt}}^T$	<i>instantaneous position vector in Cylindrical coordinates</i>
$\dot{\mathbf{x}}_{r\theta z} = [\dot{\rho}, \dot{\theta}, \dot{z}]_{\text{salt}}^T$	<i>instantaneous velocity vector in Cylindrical coordinates</i>
$\ddot{\mathbf{x}}_{r\theta z} = [\ddot{\rho}, \ddot{\theta}, \ddot{z}]_{\text{salt}}^T$	<i>instantaneous acceleration vector in Cylindrical coordinates</i>
$X_{xyz} = [x, y, z, \dot{x}, \dot{y}, \dot{z}, \ddot{x}, \ddot{y}, \ddot{z}]_{\text{salt}}^T$	<i>kinematic coordinate array in Cartesian coordinates (dot notation)</i>
$X_{xyz} = [x, y, z, v_x, v_y, v_z, a_x, a_y, a_z]_{\text{salt}}^T$	<i>kinematic coordinate array in Cartesian coordinates (symbol notation)</i>
$X_{r\theta z} = [\rho, \theta, z, \dot{\rho}, \dot{\theta}, \dot{z}, \ddot{\rho}, \ddot{\theta}, \ddot{z}]_{\text{salt}}^T$	<i>kinematic coordinate array in Cylindrical coordinates (dot notation)</i>
$X_{r\theta z} = [\rho, \theta, z, v_r, v_{\theta}, v_z, a_r, a_{\theta}, a_z]_{\text{salt}}^T$	<i>kinematic coordinate array in Cylindrical coordinates (symbol notation)</i>
q_{ρ}	<i>radial scale function</i>
m_{Ω}	<i>mass of particles included in a subdomain</i>
$\rho_{\Omega} = \frac{m_{\Omega}}{V_{\Omega}}$	<i>density of a subdomain</i>
\dot{m}	<i>mass flow rate</i>
C_c	<i>coefficient of compaction</i>

Abbreviations

FEA	<i>finite element analysis</i>
DOF	<i>degree of freedom</i>
DNM	<i>discrete numerical method</i>
IVP	<i>initial value problem</i>

List of figures

Figure 1. Spreading salt on icy road	8
Figure 2. Flat disks with different types of blades	8
Figure 3. Conical disks with different types of blades	9
Figure 4. Randomly selection of spreader disks	9
Figure 5. Mass spring damper model.....	10
Figure 6. Comparison between analytical solution and Newmark approach	11
Figure 7. Evolution of the error over time	12
Figure 8. Rock salt particles	13
Figure 9. Particle size distribution	13
Figure 10. Frames for vector kinematics.....	18
Figure 11. Definition of the velocity in the $\rho\varphi$ -plane on a spinning disk.....	19
Figure 12. Characteristic phases of the sub-cluster flow: inflow, underway and outflow.....	20
Figure 13. Sub-cluster $\Omega\Psi$ of particles discretized underway into finite sub-domains Ω	21
Figure 14. Non-stationary sub-cluster of particles moving over time	22
Figure 15. Sliding, rolling and repositioning inside a sub-cluster	23
Figure 16. Particle impacts are assumed to origin impulsive forces and moments	23
Figure 17. Camera dispositions.....	26
Figure 18. Projection of disk's edge on both planes	27
Figure 19. Relation between measurements on both planes.....	27
Figure 20. Identification of area and density sections	28
Figure 21. Distribution of salt along the blade in a particular frame	29
Figure 22. Salt particles flow	29
Figure 23. a Frame from high speed camera levelled with the disk. b. Characterization of the area of salt along the blade c. Area of a sub-domain.....	30
Figure 24. Coordinates of the required points.....	31
Figure 25. Distinction of sections with different densities	31
Figure 26. Appreciation of density distribution	32
Figure 27. Sections in the radial velocity data.....	33
Figure 28. Fit of the data with a three parameters exponential function	33
Figure 29. Film set.....	36
Figure 30. Spreader disk used	37
Figure 31. Computer setting.....	38
Figure 32. Manual setting.....	38
Figure 33. High speed camera.....	39
Figure 34. Balance KERN 440-35A.....	40
Figure 35. Timer 2002.60	40
Figure 36. Measurement of mass flow in progress	41
Figure 37. Radial velocity representation along the vane	42
Figure 38. Radial velocity of sub-domains leaving the disk	45
Figure 39. Fit function parameters	45

Figure 40. Image processing - 80rpm	52
Figure 41. Axis legend.....	53
Figure 42. Image processing - 100rpm	54
Figure 43. Axis legend.....	55
Figure 44. Image processing - 160rpm	56
Figure 45. Axis legend.....	57
Figure 46. Image processing - 190rpm	58
Figure 47. Axis legend.....	59
Figure 48. Image processing - 215rpm	60
Figure 49. Axis legend.....	61
Figure 50. Radial velocity data and model fitting - 80rpm.....	62
Figure 51. Radial velocity data and model fitting - 100rpm.....	63
Figure 52. Radial velocity data and model fitting - 160rpm.....	64
Figure 53. Radial velocity data and model fitting - 190rpm.....	65
Figure 54. Radial velocity data and model fitting - 215rpm.....	66

List of tables

Table 1. Salt spreader disk remarkable characteristics	38
Table 2. Experimental settings for the spreader unit.....	38
Table 3. High speed camera features	39
Table 4. Balance features	40
Table 5. Timer characteristics	41
Table 6. Mass flow measurements.....	41
Table 7. Collection of fit function parameters and calculation of radial velocities at the edge of the disk	42
Table 8. Summary of the goodness of fit coefficients evaluated.....	43
Table 9. Cylindrical coordinates of the points of interest - 80rpm.....	53
Table 10. Mass flow estimate – 80rpm	53
Table 11. Line segments parameters m and c – 80rpm.....	53
Table 12. Coefficient of compaction distribution – 80rpm	53
Table 13. Division of density sections – 80rpm.....	53
Table 14. Cylindrical coordinates of the points of interest - 100rpm	55
Table 16. Line segments parameters m and c – 100rpm	55
Table 15. Mass flow estimate - 100rpm	55
Table 17. Coefficient of compaction distribution – 100rpm	55
Table 18. Division of density sections – 100rpm.....	55
Table 19. Cylindrical coordinates of the points of interest - 160rpm	57
Table 20. Mass flow estimate - 160rpm	57
Table 21. Line segments parameters m and c – 160rpm	57
Table 22. Coefficient of compaction distribution – 160rpm	57
Table 23. Division of density sections – 160rpm.....	57
Table 24. Cylindrical coordinates of the points of interest - 190rpm	59
Table 26. Line segments parameters m and c – 190rpm	59
Table 25. Mass flow estimate - 190rpm	59
Table 27. Coefficient of compaction distribution – 190rpm	59
Table 28. Division of density sections – 190rpm.....	59
Table 29. Cylindrical coordinates of the points of interest - 215rpm	61
Table 30. Mass flow estimate - 215rpm	61
Table 31. Line segments parameters m and c – 215rpm	61
Table 32. Coefficient of compaction distribution – 215rpm	61
Table 33. Division of density sections – 215rpm.....	61

Table of contents

1. Introduction	8
1.1. Context	8
1.2. Numerical methods	10
1.3. Problem domain	12
1.4. Salt characteristics	13
1.5. State of the art	14
1.6. Objectives	17
2. Method	18
2.1. Introduction to methods and principles	18
2.1.1. Notation.....	18
2.1.2. Sub-cluster behavior.....	19
2.1.3. Characterization of sub-cluster kinematics.....	21
2.1.4. Parameterization of sub-cluster kinematics.....	23
2.2. Data acquisition from high speed videos	25
2.2.1. Plane projections	26
2.2.2. Considerations taken to obtain radial velocity data	28
3. Results	36
3.1. Introduction to results	36
3.2. Equipment and data processing	37
3.2.1. Tractor.....	37
3.2.2. Salt spreader unit	37
3.2.3. High speed camera.....	39
3.2.4. Balance	40
3.2.5. Timer	40
3.2.6. Mirror.....	41
3.3. Flow measurements and considerations	41
3.4. Radial scaling functions	42
4. Discussion	44
4.1. Perspectives and un-answered questions	44
4.2. Conclusion	45
5. References	47
5.1. Literature	47
5.2. Software	50
6. Annexes	51
6.1. Frame processing	51
6.1.1. Rotation speed of the disk: 80 rpm	52

6.1.2.	Rotation speed of the disk: 100 rpm	54
6.1.3.	Rotation speed of the disk: 160 rpm	56
6.1.4.	Rotation speed of the disk: 190 rpm	58
6.1.5.	Rotation speed of the disk: 215 rpm	60
6.2.	Extracted data for the radial velocity and model fitting	62
6.2.1.	Rotation speed of the disk: 80 rpm	62
6.2.2.	Rotation speed of the disk: 100 rpm	63
6.2.3.	Rotation speed of the disk: 160 rpm	64
6.2.4.	Rotation speed of the disk: 190 rpm	65
6.2.5.	Rotation speed of the disk: 215 rpm	66
6.3.	MATLAB® codes	67
6.3.1.	Analytic solution vs Newmark average acceleration solution	67
6.3.2.	Newmark average acceleration algorithm	68
6.3.3.	Newmark approach incorporating radial scaling function	69
6.3.4.	Obtaining of the radial velocity and fitted models	71
6.3.5.	Modeling of rotating spreader disk with straight blades	72

1. Introduction

1.1. Context

Salt is spread on the roads every year to combat the winter effects of ice and snow which make the roads dangerous for driving (Figure 1). Basically, salt works by lowering the freezing point of water on the road. The most common system to spread salt on roads is the spinning disk in its different variants. Its popularity is motivated by its low cost to produce, its large spread width, small size and simple construction (Aphale et. al, 2003).



Figure 1. Spreading salt on icy road (BREDAL A/S 2014)

The spinner spreader consists of a rotating disk with blades fixed to the disk surface. The salt is poured onto the spreader disk colliding with the rotating blades before finishing on the ground.

There is a vast variety of spreader disks (Figures 2 and 3). Normally, they are distinguished according to whether they have a conical or flat disk, with radial or pitched, curved or straight vanes.



Figure 2. Flat disks with different types of blades (Agrex S.p.A., 2014; Rauch, 2013)

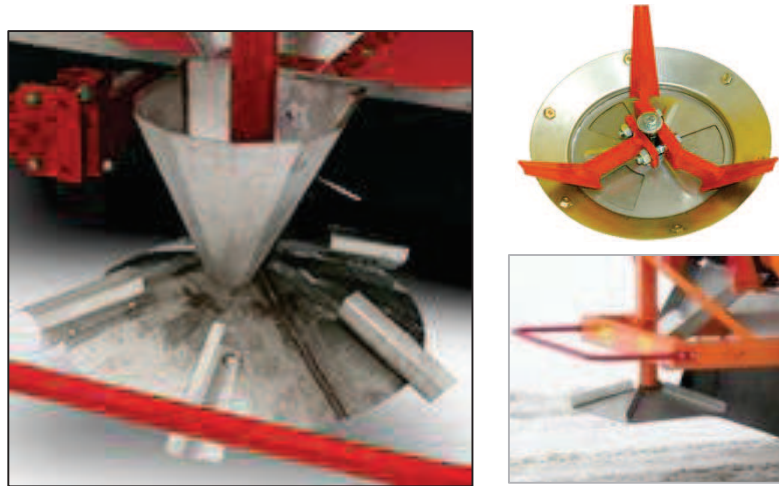


Figure 3. Conical disks with different types of blades (BREDAL A/S, 2014; Agrex S.p.A., 2014; UNIA in Romania, 2013)

Furthermore, spreader disks are characterized by their number of blades, geometry of the vanes, diameter of the disk, angle of the disk and material composition (Figure 4).



Figure 4. Randomly selection of spreader disks (Agrex S.p.A., 2014; BREDAL A/S, 2014; Bogballe, 2014; Agriaffaires, 2014)

The performance of these devices is highly dependent on the weather, the particle characteristics of the de-icing material and the machinery settings. Due to the significant financial implications of inaccurate spreading, a large number of scientists (Yule, 2011; Van Liederke et al., 2009; Inns & Reece, 1962) have focused their research on studying the spreader disk. Numerous steps towards the characterization of the whole spreading process have been carried out (Tijskens et al., 2004; Grift & Kweon 2006), but there are still many unanswered questions. This work intend to shed some light on the understanding of the spreading process with respect to the interplay of the rotation velocity of the disk and the evolution of the radial velocity of a sub-cluster of salt particles on the disk.

Trial and error is expensive and time consuming, hence the motivation to create a mathematical model is appealing. Focus is on the movement of the salt on the spreader disk based on classical Newtonian mechanics and some assumptions that incorporate the definition of a scaling function (chapter 2: methods). The work is still at its first stage, however the model is expected as a tool to obtain reductions in the cost and time required to optimally design spreader disks in the future.

1.2. Numerical methods

The modelling of the motion of a salt sub-cluster in a spreader disk involves complex physics that seems to be stochastic by nature. Therefore, analytic solutions are out of reach and one has to lean against approaches that can be based on numerical time integration methods.

Different numerical methods are investigated for the numerical evaluation of the dynamic response of the spinning disk system that is in focus in this study. The methods taken under consideration to affront this problem have been: the Newmark method, the central difference method, the Wilson θ method and the Houbolt method.

Two fundamental concepts have been considered when choosing which method would be the most suitable for the studied case: stability and accuracy of the integration scheme. Several authors have studied these four methods along the time, providing representative data and comparisons between them (Xie, 1996; Villar, Menezes & Donadon, 2012). In general, researchers agree that the Newmark constant acceleration method is recommended for a dynamic analysis of a non-linear system. The Newmark scheme is also included in the novel sub-cluster approach and therefore its key aspects are described hereafter.

The Newmark method in its average acceleration variant is based on the assumption that the acceleration of the system can be taken as the average value between two successive points of the particle's trajectory. The Newmark average acceleration method defines the following expressions for acceleration, velocity and position in every time step Δt as:

$$\ddot{\rho}_\tau = \frac{(\ddot{\rho}_{t_0} + \ddot{\rho}_{t_0+\Delta t})}{2} \quad \text{Where:}$$

$$\dot{\rho}_{t_0+\Delta t} = \dot{\rho}_{t_0} + \ddot{\rho}_{t_0}(1 - \gamma)\Delta t + \Delta t \gamma \ddot{\rho}_{t_0+\Delta t} \quad \beta = \frac{1}{4}$$

$$\rho_{t_0+\Delta t} = \rho_{t_0} + \dot{\rho}_{t_0} \Delta t + \ddot{\rho}_{t_0} \left(\frac{1}{2} - \beta\right) \Delta t^2 + \Delta t^2 \beta \ddot{\rho}_{t_0+\Delta t} \quad \gamma = \frac{1}{2}.$$

The efficiency of the Newmark method has been tested on a classical radial SDOF system by comparing Newmark's numerical solution to the system's well-known analytical solution, see Figure 5.

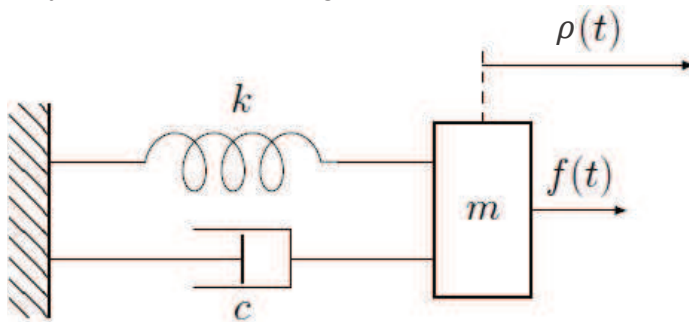
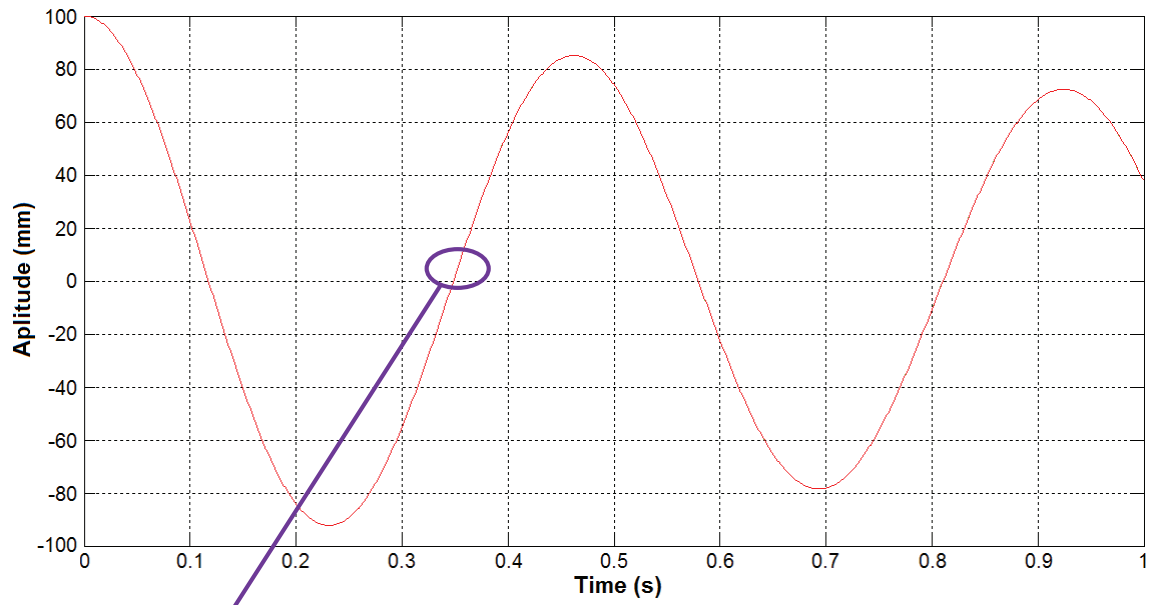


Figure 5. Mass spring damper model

$$m \ddot{\rho} + c \dot{\rho} + k \rho = f(t)$$

$$\begin{aligned} \Delta t &= 0.001 \text{ s} \\ k &= 1850000 \text{ N/m} \\ c &= 7000 \text{ N s/m} \\ m &= 10000 \text{ kg} \\ t &= 1 \text{ s} \\ \rho_{t_0} &= 100 \text{ mm} \\ \dot{\rho}_{t_0} &= 0 \text{ mm/s} \\ f(t) &= 0 \text{ N} \end{aligned}$$

Where, m , c and k denote the mass, damping and stiffness components. $f(t)$ represents the forces acting on the mass, t the time in a time window $t \in [t_{beg}, t_{end}]$ and $\{\rho, \dot{\rho}, \ddot{\rho}\}$ the radial motion variables.



■ Newmark method ■ Analytical solution

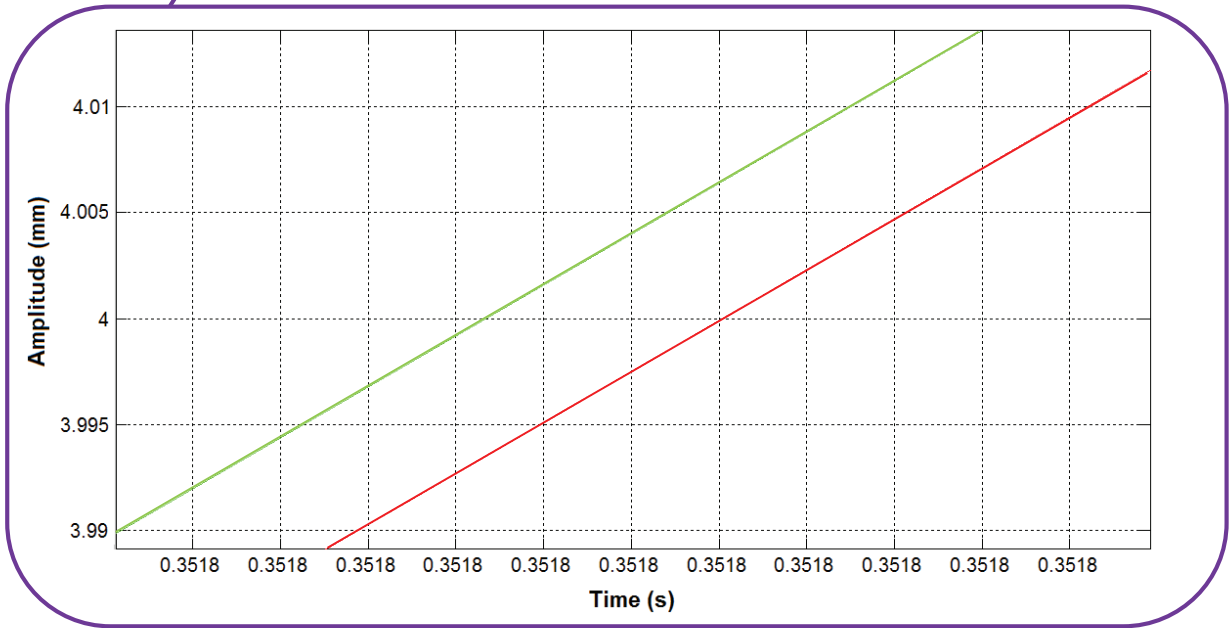


Figure 6. Comparison between analytical solution and Newmark approach

For the SDOF system considered, Figure 6 illustrates the distinct amplitude solutions for the Newmark numerical solution and the analytical solution.

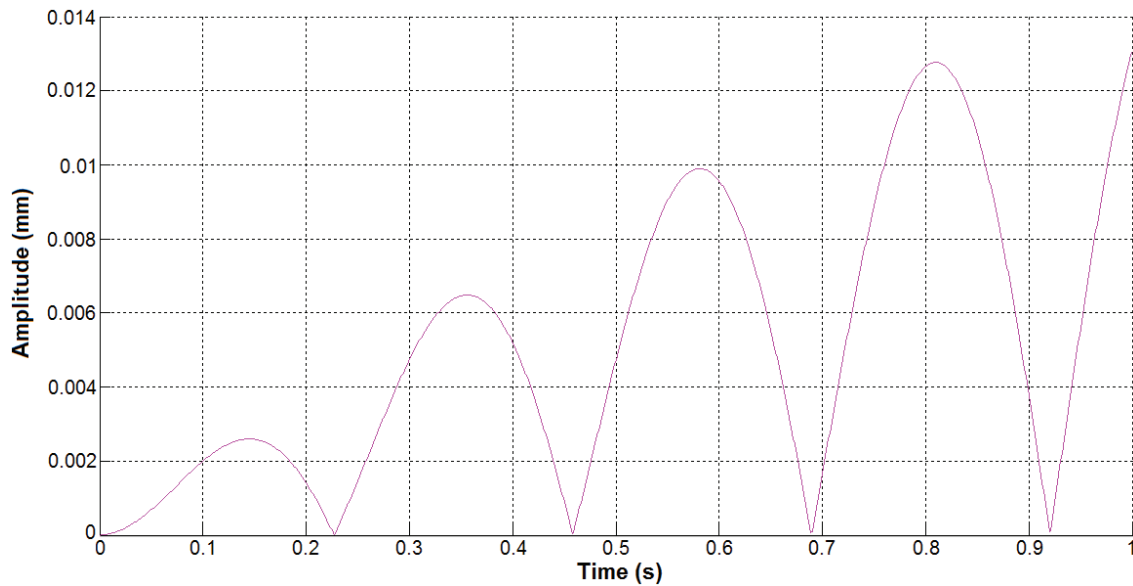


Figure 7. Evolution of the error over time

In Figure 7, the deviation between numerical and analytic solution is defined as the absolute difference between the distinct solutions. This gives a simple representative view of the error over time.

It is seen that the error grows over time. In a 1 second time window it is reached a maximum absolute error of 0.013 mm and a maximum relative error of 0,03439% defined as the ratio of the maximum absolute error to the accepted measurement (analytical solution) at the time the absolute error is maximum. Taking into account that the minimum disk velocity considered is 80 rpm, (i.e. slightly more than 1,3 turns per second), there is no need to analyse a bigger time window since it by experience is known the salt sub-cluster leaves the disk in less than a whole revolution.

1.3. Problem domain

The observation of high speed videos of spinning disks spreading salt gives an idea about the flow complexities due to sliding, rolling and repositioning of the salt particles along their trajectory on the disk. A novel kinematic approach formulated on the basis of shape functions intends implicitly to incorporate these non-stationary flow complexities.

The mentioned kinematic shape function, includes a radial scaling function that allows for a sub-cluster approach of salt particles in the spinning disk rather than the conventional approaches that develop their models from the behaviour of a single particle (Patterson & Reece, 1962; Inns & Reece, 1962; Mennel & Reece, 1963).

1.4. Salt characteristics

The common type of salt used for de-icing of roads is called rock salt, also known as halite. Its chemical composition is sodium chloride (NaCl) and it is widely used due to its high availability and exceptional ice melt properties (Salt Association, 2014).

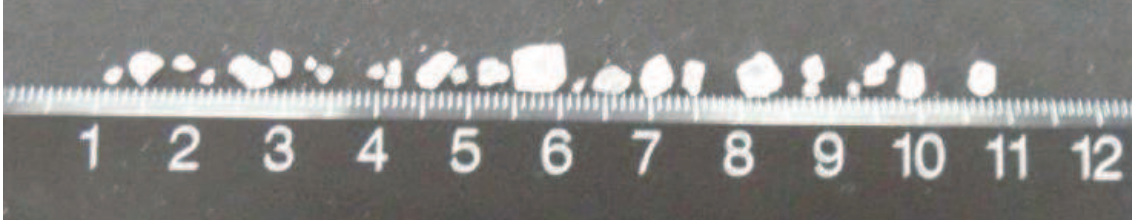


Figure 8. Rock salt particles (Takai, 2013)

As seen in Figure 8, the size and shape of salt particles show a large variation. The density of salt considered in this study is 2165 kg/m^3 (Weast & Astle, 1981-1982).

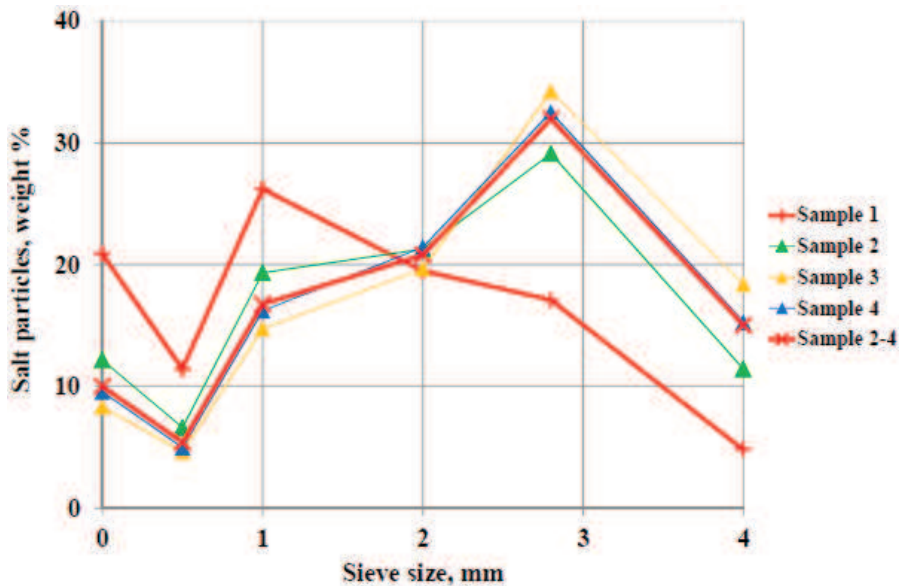


Figure 9. Particle size distribution (Strøm 2012a, Strøm 2012c)

The particle size distribution has been studied from several samples of salt taken from the top of the hopper and from the salt conveyer of the salt spreader unit by (Strøm, 2012a; Takai, 2013) Their findings, see Figure 9, are included in this study since they used the same salt spreader unit and the same type of salt in their research that has been used here.

1.5. State of the art

The performance of spinning spreader disks has been widely investigated (Patterson & Reece, 1962; Hao, Jianqun & Hong, 2013; Brochner & Macías, 2014). Abundant are the papers which analyse fertilizer spread and less are the ones with salt as object of the investigation. Nevertheless the physics behind the movement of both materials on the spreader disk is comparable. Therefore, in order to be aware of the current status and recent achievements in the field, research about salt spread on roads as well as about fertilizer distribution with agricultural purpose have been studied.

The object of study has been quite varied. While many authors have developed analytical models of the particles on the disk or/and on the air before landing on the ground, others have focused their research on identifying which factors influence the spread pattern. Meanwhile, another group of authors have paid more attention to determine the velocity and the direction of the particles in the proximity of the disc. Also, a considerable number of authors have led their effort to elaborate simulations based on discrete element methods (DEM).

(Patterson & Reece, 1962) studied the motion of a single spherical particle on a flat spreader disk with radial straight blades. They distinguished between rolling and sliding motion of the particles. The analytical models developed assumed a near-centre feed and neglected bouncing of particles against the blades. A comparison between these models and experimental data got using steel ball bearings showed reasonable agreement on the radial and total velocities of the particles leaving the disk as well as on the angle between where particles fall and where they leave the disk. (Inns & Reece, 1962), used the same disk configuration and took into account the existence of impacts between the particle and the blade and developed their model for an off-centre feed. The model developed satisfied steel ball bearings movements but performed poorly when studying irregular shape particles. (Cunningham, 1963) separately developed models for a flat disk with straight and curved blades and for concave disks. A couple of years later, (Cunningham & Chao, 1967) proved the consistency of the models by getting experimental data of the angle at which various fertilisers left the disk.

Abundant are the research focused on developing models for off-spinner particle trajectories interested in the motion of the particle through the air after being release of the spreader disk. Keeping this in mind, (Reints & Yoerger, 1967) made a simulation of the trajectory of a particle through the air. (Mennel & Reece, 1963) describe the trajectory for an off-spinner particle considering a non-horizontal release. They studied both spherical and irregularly-shape particles analytically but they only got experimental data using steel ball bearings. They claim good agreement between model and experiments. (Pitt, Farmer & Walker, 1982) simplified the off-spinner expressions of motion to determine particle trajectories through the air, they obtained an error less than 7% between their solution and the model of (Mennel & Reece, 1963).

The models described above have been base for several simulation studies. (Griffis, Ritter & Matthews, 1983) based their simulations of the trajectory of the particle on the disk upon the model of (Patterson & Reece, 1962). They made a comparison between their predicted spread patterns and experimental data using two types of fertilizers and did not find good agreement. They blamed particle interactions and irregularly-shaped particles of the discrepancies found. (Olieslagers, Ramon & De Baerdemaeker, 1996)

also attributed the abundant discrepancies between their predicted spread pattern and their experiments to particle interactions. They gathered data from a spreader manufacturer and compare it to simulations developed for the same fertilizer and spreader. In order to improve the results they tried to introduce several parameters in the simulation with little success until they took into account the importance of the situation on the disk where the particles drop down. When using a set of parameters representing the landing area of particles the simulation was remarkably improved. (Dintwa et al., 2004b; Dintwa et al., 2004a) also include the 'landing area' parameter in their simulations to satisfactorily predict spreader distribution patterns for a conical disk equipped with pitched vanes. The model was derived as a generalisation of an earlier model which could only characterize particle motion on a flat disk with radial blades. These authors determined statistically a distribution pattern by treating the collective flow as a superposition of a large number of particles motion varying their initial positions on the disk. Another analytical solution of a particle motion on a concave disk spreader with pitched blades was presented by (Villette et al., 2005). The new form for the differential equation proposed is in agreement with the model elaborated by (Patterson & Reece, 1962) and (Cunningham, 1963). However, it shows some discrepancies with the model stated by (Dintwa et al., 2004b).

Multitude factors have been identified as having influence on the spreader pattern from a spinner disk dedicated to distribute fertilizer or salt. These can be divided in three main sections: the environment where the spreading takes place, the machine in charge of the spread and the material spread's characteristics. A small number of authors have studied the effect of factors from the three categories in the same report, such as (Olieslagers, Ramon & De Baerdemaeker, 1996) who identified environmental factors with influence on the spread pattern, created a relation between several machine factors and their fertilizer distribution quality and also identified a number of particle characteristics. (Strøm, 2012a; Strøm, 2012c; Strøm, 2012b) focused their effort on the characterization of environmental factors, specifically air movement. Therefore, they studied the effect of cross wind, drafts created behind the truck and methods to maintain desirable shape on the resulting distribution pattern. Numerous are the researchers who have dedicated their works to analyse the relation between machine features and spread patterns. (Dintwa et al., 2004a) used a custom-made prototype spreader for calibrating their model for changes in several spreader settings. Thus, they were able to quantify the influence of spreader adjustments such as mass flow, disk width, rotation speed, blade pitch radius or orifice radial dimensions on the spread pattern. (Pitt, Farmer & Walker, 1982) found that the drop location of the particle have big influence on the spread patterns. (Griff & Kweon, 2006) arrived to the same conclusion, they proved using simulations that it is possible to get highly uniform shapes of the fertilizer spread pattern by changing the drop location of the particles around the centre of the disk. (Fulton et al., 2001), using the ASAE 341.2 standardized collection tray method, developed a deep investigation on the flow rate of fertilizer. They observed a desirable bell shape spread pattern when using a low application rate, a mediocre M-shape at medium values and an undesirable W-shape when performing with high application rates. (Villette et al., 2012) experimented with changes in mass flow and rotational speed and reported consistent data regarding their effect on the spread pattern. Results showed that the standard deviation of the distribution of fertilizer increases with the mass flow and decreases with the rotational speed. The last category is composed by authors who

focused their investigations on identifying which fertilizer characteristics change spread patterns. For this purpose, (Hofstee & Huisman, 1990) investigated the influence of some factors on particle motion on and off the disk. Characteristics of fertilizer such as particle size distribution, coefficient of friction, coefficient of restitution, particle strength and aerodynamic resistance. (Yule, 2011) concentrated on studying the effect that particle size distribution has on the spread pattern. The analysis of 1700 tray samples revealed the effect small particles have on the pattern. As the proportion of small particles increases, the pattern peak around the centre line of the spreader does as well. Nevertheless, the author claims that if the proportion of particles smaller than 0,4mm remains below 15%, the coefficient of variation of spread is not disturbed in more than a 5%.

Regarding measurements of the velocity and the direction of the particles once they leave the disk, several methods have been developed based on ultrasonic transducers (Hofstee, 1994 & Hofstee, 1995), photo sensitive sensors (Griff & Hofstee, 1997), high speed videos (Olieslagers, 1997), traditional photography (Reumers, Tijskens & Ramon, 2003; Olieslagers, 1997), stroboscopic methods (Cointault, Sarrazin & Paindavoine, 2002; Vangeyte et al., 2004), use of a CCD camera to create an imaging system (Van Liedekerke et al. 2008) or kinematic analysis (Villette et al., 2008).

Another frequent approach to simulate spreading patterns is the use of discrete element methods (DEM) what is currently gaining devotees because the computational power needed is becoming more and more available lately. The general DEM was originally developed by (Cundall, 1971) to study movements in rocky systems and nowadays is applied in many fields. A DEM is any of a family of numerical methods that, inspired by molecular dynamics, is able to compute the motion and mechanical behaviour of a large number of small particles. Ideally suited for simulating phenomena related to granular flows, DEM summarize the forces acting on the particles and integrate over time the Newton's equations of motion. Thereby, the method predicts the trajectory of every particle in the whole over time and the forces it suffers. Therefore, this technique is capable to deal with a complete stream of particles on and off the spreader disk.

DEM simulations have been used widely to study mixers (Stewart et al., 2001; Zhou et al., 2004; Kuo et al., 2004), systems similar to spinning disk providing good results. Besides, DEM have also been applied in many investigations of the motion of particles on a spinning disk. (Van Liedekerke et al., 2008) develop a model using the DEMeter++, C++ software library which offer a wide toolkit for the production of Particle Based Simulation programs in short time (Tijskens et al., 2004). The comparison between DEM simulations and experimental data was extremely satisfactory.

Van Liedekerke et al. created a series of papers based on the laws of physics with the aim of simulating the complete spreading process proposing to incorporate the interactions between particles in their models. They performed a DEM analysis model of the motion of one single particle of fertilizer in a spinning disk. First in a flat disk with two radial vanes (Van Liedekerke et al., 2006) and a couple of years later they study two more complex geometries: a lawn flat spreader disk with four straight blades and a field spreader disk with a conical inclination of 9° equipped with two L-shaped blades (Van Liedekerke et al., 2009). Comparing analytical formulas and experiments with DEM simulations they found a good agreement. More specifically, they claimed to predict the spread pattern with a deviation below a 5% for low outlet velocities of the particle (10

m/s). For higher speeds the deviations increase and the simulations lose their ability to predict spread patterns accurately. They also suggested in their papers to have some disagreements with (Patterson & Reece, 1962) and their predictions.

1.6. Objectives

The objective of this study is to:

- Develop an algorithm that can predict the mean value flow of rock salt particles from characteristics parameters of a simple spreader disk design.
- To validate the predicted flow from observations on high speed videos of the real salt flow in a full-scale salt spreader disk.

2. Method

2.1. Introduction to methods and principles

In this chapter, key aspects for sub-cluster modelling are introduced and followed by introductory elements of Newtonian sub-cluster mechanics.

The main hypothesis of this work is that a kinematically feasible shape function exists that can be parametrically fitted to observed sub-cluster flows by a radial scaling function. In this regard, a novel detection algorithm is developed to obtain transcendental data from the high speed videos and use them to estimate the parameters of the radial scaling function.

To validate the hypothesis, high speed videos of the spinning disk spreading salt at five different rotation speeds are analysed and their goodness of fit characteristics are outlined.

2.1.1. Notation

In general, notation for discretization is taken from (Brøchner, 2013) and supplemented with notations for space and time in accordance with ISO 80000-3:2006(E). Notation for mechanics is in accordance with ISO 80000-4:200(E) and is supplemented with special terms relevant for the description of spinning salt spreaders.

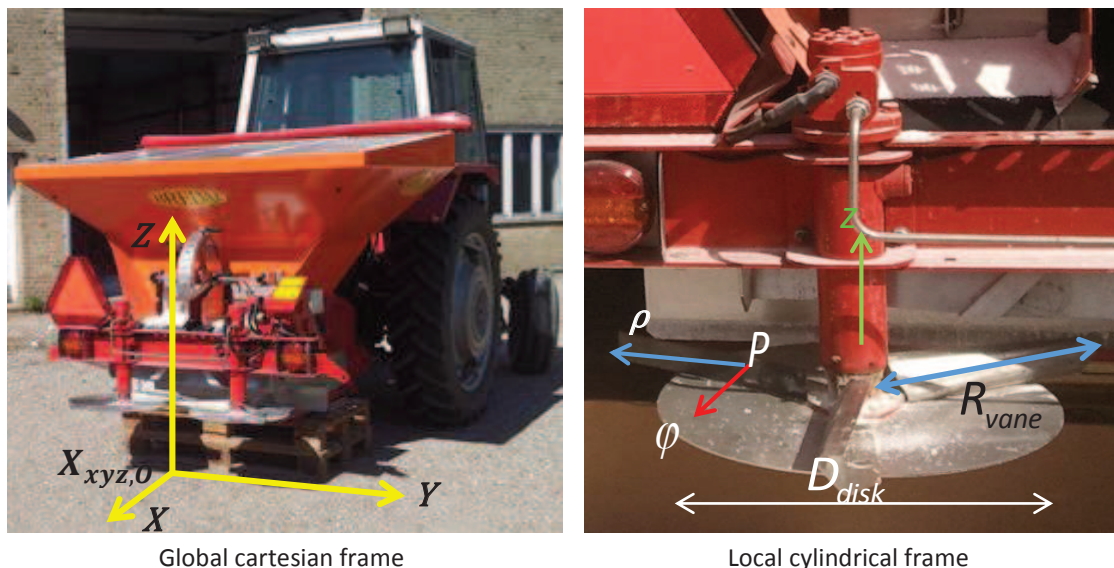


Figure 10. Frames for vector kinematics

Figure 10 illustrates the global Cartesian frame (left) with origin at road level at the centre of the rear end of the spreading vehicle and with its vertical Z axis upwards. Furthermore it defines the local Cylindrical frame (right) with local origin typically 0.4 meter above ground. The local system is oriented with a vertical z-axis of rotation (green) and its radial axis is directed outwards (blue) and perpendicular to z. This means, that the global Z axis and the local z-axis coincide. The disk is defined to have a positive angular speed

when the disk is spinning counter clockwise around the local z-axis in accordance with the conventional right-hand rule.

Furthermore, the geometry of the spreader disk is defined through its outer diameter D_{disk} and its maximum vane radius R_{vane} .

The global stationary origin $\mathbf{x}_{xyz,0}$ is defined at road surface in Cartesian coordinates, i.e.:

$$\mathbf{x}_{xyz,0} = [x_0, y_0, z_0]^T.$$

The kinematics of any point P on the disk is defined in a local Cylindrical frame with position, velocity and acceleration vectors given by the well-known formulas:

$$\mathbf{r}_{\rho\phi z} = [r_\rho, r_\phi, r_z]^T = [\rho, \phi, z]^T$$

$$\mathbf{v}_{\rho\phi z} = [v_\rho, v_\phi, \dot{z}]^T = [\dot{\rho}, \rho\dot{\phi}, \dot{z}]^T$$

$$\mathbf{a}_{\rho\phi z} = [a_\rho, a_\phi, \ddot{z}]^T = [\ddot{\rho} - \rho\dot{\phi}^2, \rho\ddot{\phi} + 2\dot{\rho}\dot{\phi}, \ddot{z}]^T$$

- **Steady Rotation**

For conventional spreader disks in operation the angular velocity $\dot{\phi}$ is usually not varying. A constant angular velocity ω also means that the angular acceleration $\ddot{\phi}$ can be assumed to be zero, i.e.:

$$\dot{\phi} = \text{Const} = \omega \rightarrow \ddot{\phi} = \frac{d\dot{\phi}}{dt} = 0$$

Therefore, for a spinning spreader disk the velocity description in the $\rho\phi$ -plane can be completely defined by motion variables $\{\rho, \dot{\rho}, \dot{\phi}\}$ that originates from the radial direction only (obviously including the z-direction as well), i.e. the angular variables are absent.

$$\mathbf{v}_{\rho\phi} = [v_\rho, v_\phi, \dot{z}]^T = [\dot{\rho}, \rho\omega, \dot{z}]^T$$

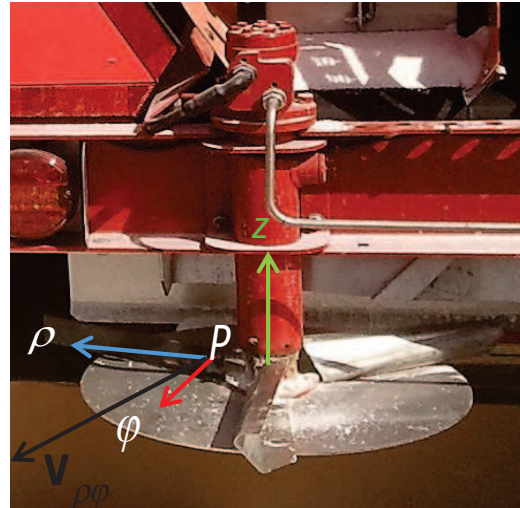


Figure 11. Definition of the velocity in the $\rho\phi$ - plane on a spinning disk

2.1.2. Sub-cluster behavior

Instead of using old-fashion single particle approaches, this research is focused in studying the behaviour of a sub-cluster of salt particles in a spinning spreader disk. It is

observed that the flow of particles can be described as a sub-cluster that contains a varying number of particles. The sub-cluster starts grooving from when the first particle drops down on the disk. Then more particles follow and when the fan reaches the first particle on the disk it starts collecting them at its front. More and more particles are collected and at a certain stage, particles located at the tip of the fan start leaving the spreader. More particles follow and finally all particles have left the spreader. However, since the particles leave the spreader over only a proportion of a full turn, the outflow is characterized by a full sub-cluster of particles that forms a swarm.

The sub-cluster flow of particles is separated into three phases: inflow, underway and outflow as it can be seen in the following figure.

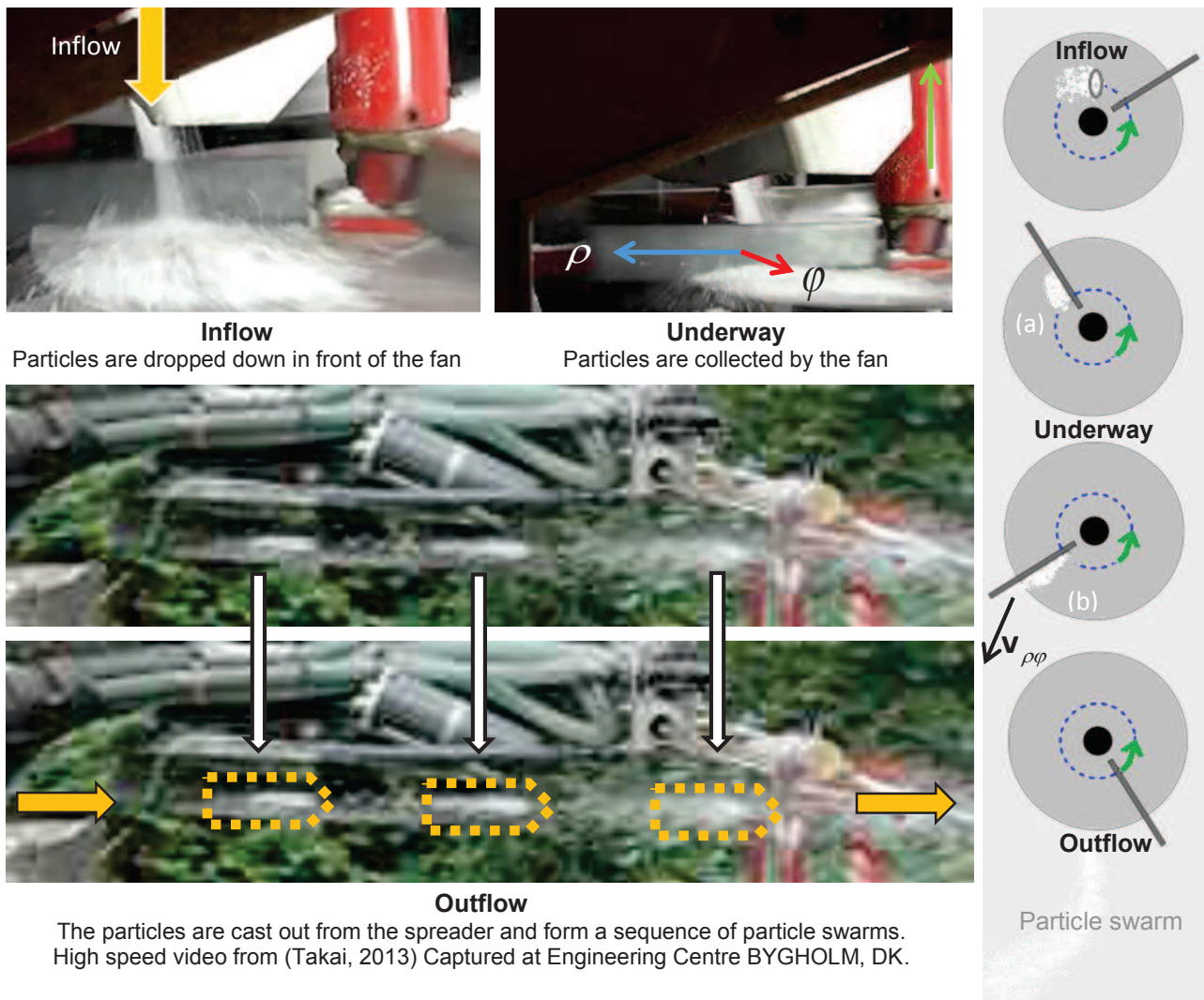


Figure 12. Characteristic phases of the sub-cluster flow: inflow, underway and outflow

Figure 12 illustrates how the salt is dropped onto the spinning disk (inflow), caught up by the vane (underway) and finally cast out as particle swarms (outflow). During the inflow particles build up on the rotating disk in front of the blade. Underway (a), when the blade collects the particles a non-stationary irregular sub-cluster is formed. At a following stage (b) the particles start leaving the disk and finally, after all particles have left the disk, their

motion in the air can be regarded as a particle swarm¹. The inflow is constant, however during one turn the sub-cluster flow transforms from a continuous inflow to a discontinuous outflow.

2.1.3. Characterization of sub-cluster kinematics

In the sub-cluster model presented in Figure 13, shown in a local frame of reference in cylindrical coordinates $\rho\varphi z$, the salt particles collected by one vane of a spinning spreader disk are assumed to form a non-stationary space time constellation represented by a time dependent sub-cluster $\Omega_\psi(t)$.

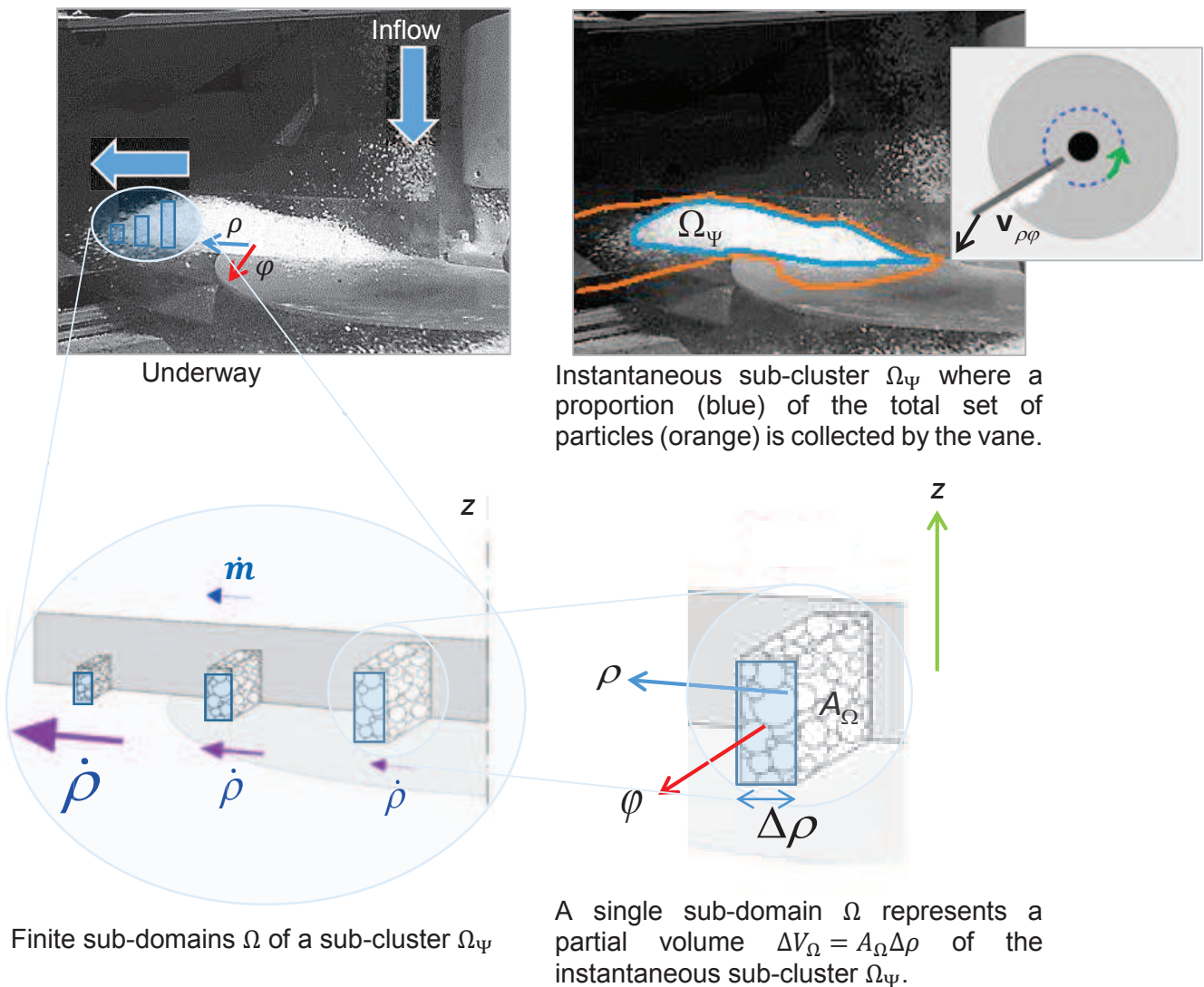


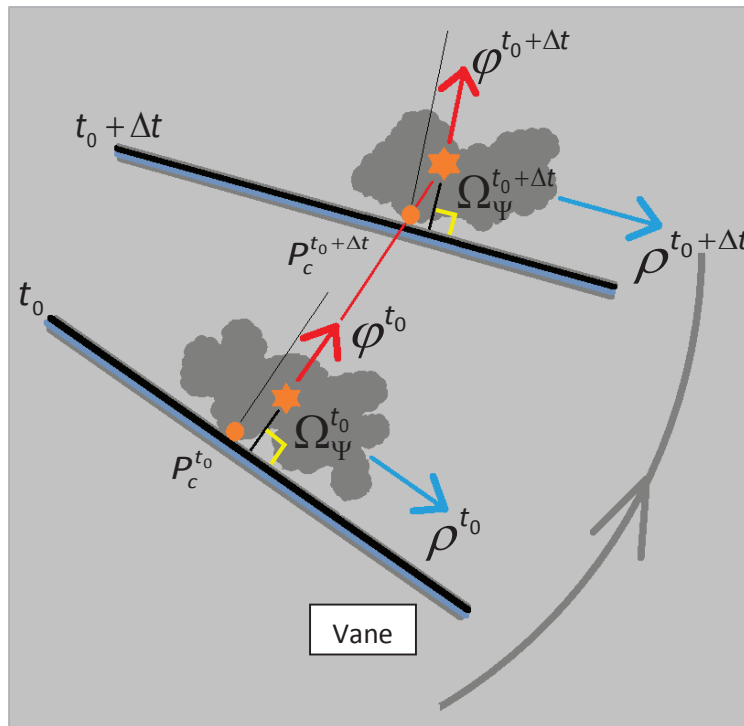
Figure 13. Sub-cluster Ω_ψ of particles discretized underway into finite sub-domains Ω

¹If the spreader is designed with three fans then three swarms are generated per turn. Also note that when the spreader disk is rotating with a high number of revolutions per minute the salt swarms cannot be recognized by the human eye; however when spreading is recorded by high speed camera, the salt swarms become clearly visible.

In the previously described model, the sub-cluster Ω_Ψ is discretized into small sub-domains Ω that are characterized by having a homogenous mass flow inside their finite volumes V_Ω . Each volume is assumed to be represented by its length $\Delta\rho$ and area A_Ω . Assuming that the volume of each subdomain goes towards zero the internal mass-distribution is substituted by the total sub-domain mass located at the instantaneous subdomain centre of mass.

In a polar $\rho\varphi$ -frame, Figure 14 illustrates the complex motion of a sub-cluster Ω_Ψ . Although sub-clusters are supposed to have several contact points between the blade and the disk, only a single point with the blade is included in the illustration.

Over a time window $[t_0, t_0 + \Delta t]$, as the geometry of the sub-cluster is non-stationary, the location of the contact point (orange bullet) as well as the internal constellation of the sub-cluster is assumed to vary. The variation in the location of the impact points is supposed to be caused by sliding, rolling and repositioning of the particles as it can be seen in high speed videos observing the movement of the particles in the close neighbourhood of the vane.



Furthermore, for a sub-cluster with a single contact point it must be anticipated that the sub-cluster centre of mass (orange star) is not located at the contact point between the vane and the transverse axis. Instead it is assumed that the ever changing centre of mass is located at a line parallel to it.

Figure 14. Non-stationary sub-cluster of particles moving over time

In Figure 15 the complex motion of salt particles including sliding, rolling and repositioning of salt particles is illustrated. Physically, it is assumed that friction forces and elastic forces are driving this behaviour. Therefore, in a small scale, the nature of this motion could be categorized as impulsive. Figure 16 illustrates the integral effect of such corresponding impulsive forces (F) and moments (M).

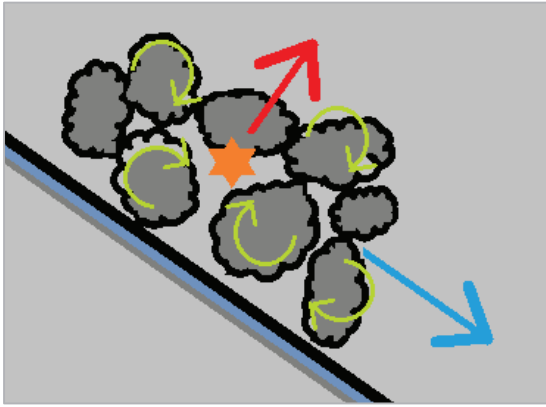


Figure 15. Sliding, rolling and repositioning inside a sub-cluster

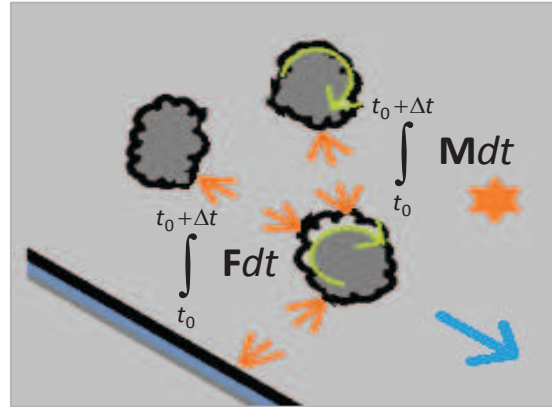


Figure 16. Particle impacts are assumed to origin impulsive forces and moments

The model details that are going to be described hereafter implicitly include such effects from sliding, rolling and repositioning of the salt particles (Brochner & Macías, 2014).

2.1.4. Parameterization of sub-cluster kinematics

- **A novel kinematic shape function that implicitly include complex cluster kinematics**

In this section, a novel kinematic shape function is introduced. The name *shape function* is taken from FEA. However here it does not represent a function that is to be super positioned by other shape functions but rather a mathematical definition of the kinematics that can be customized by the modeller. The novel kinematic shape function is expected to give a physical interpretation from classical Newtonian mechanics and intends to incorporate the non-stationary flow complexities due to sliding, rolling and repositioning of the particles inside sub-clusters.

The key idea is that the kinematics for the centre of masses for each sub-domain can be described by a kinematic shape function that can be customized parametrically to fit observations of real spreader flows recorded by high speed cameras.

The aim is to define a multiparametric function that is very flexible, which means that the same function must be able also to describe irregular trajectories of points on a spinning disk by adjusting just a few parameters. However, the kinematic shape function must be defined so that the position, velocity and acceleration functions can be predicted at any point on the radial axis. In other words, the novel shape function is simply a mathematical function that can be adjusted parametrically to predict the motion at any point of a spreader disk during one turn of revolution.

From a mechanics perspective, the shape function must comply with classical kinematics and incorporate a feasible description of the classical kinetics that implicitly includes sliding, rolling and repositioning of particles. That means that the approach must include,

at least in a mean value approach, the effects from impulsive forces and moments and their derived changes in linear and angular momentum illustrated in Figure 16.

- **A kinematically feasible approach**

An ongoing study by (Brochner & Macías, 2014) focusses on the parameterization of sub-cluster motion of particles in spreader disks. The proposed methodology includes a kinematic prediction function $\hat{f}(t_0, \Delta t, \hat{q}_\rho^{t_0+\Delta t})$ that is based on a *kinematically feasible approach* as illustrated in Figure 14. The background theory is defined in details in (Brochner & Macías, 2014). However, the prediction function is represented as a one-step implicit DNM that predicts the kinematic solution $X^{t_0+\Delta t}$ at time $t = t_0 + \Delta t$, of the governing IVP for the cluster motion from given “initial” values X^{t_0} at time t_0 . The overall objective is to refine the prediction function in a way that enables reliable estimates for the entire 3D-kinematics of spreader disks. However, in the ongoing piloting study by (Brochner & Macías, 2014) the kinematics is restricted to the radial direction only and the corresponding 1D radial prediction function is defined as:

$$X_\rho^{t_0+\Delta t} = f(X^{t_0}, \Delta t, \hat{q}_\rho^{t_0+\Delta t}),$$

where the parametric sub-function $\hat{q}_\rho^{t_0+\Delta t}$ is called the *radial scaling function*.

The radial scaling function is used to fit full-scale video-observations from high speed cameras so the predicted and observed radial velocities do not differ significantly for a predefined range of arbitrary speeds of rotation. In general, the radial scaling function depends on radius, angle and time, i.e.:

$$\hat{q}_\rho^{t_0+\Delta t} = \hat{q}_\rho^{t_0+\Delta t}(\rho(\varphi(t)))$$

- **Theoretical delimitations**

However, in the MSc-project reported in this thesis the focus is delimited to the *radial scaling function* $\hat{q}_\rho^{t_0+\Delta t}$ for a characteristic angle $\varphi^* = \varphi(t = t^*)$ at a characteristic instant of time ($t = t^*$), i.e.

$$\hat{q}_\rho^{t_0+\Delta t} = \hat{q}_\rho^{t_0+\Delta t}(\rho(\varphi^*))$$

Furthermore, the radial scale function is fitted only to observed radial velocities.

- **The fitting process**

The correspondence between observed radial velocities $\dot{\rho}_{\text{obs}}^{t_0+\Delta t}$ and simulated values $\dot{\rho}^{t_0+\Delta t}$ is based on observed video frames and computer simulated predictions respectively. The observed video data originates from high speed videos whereas the Newmark prediction scheme is used to predict the position, **velocity** and acceleration.

Algorithmically, the Newmark scheme is implemented from second order perturbations and defined in the radial direction as:

$$X_{\rho}^{t_0+\Delta t} = \begin{bmatrix} \rho^{t_0+\Delta t} \\ \dot{\rho}^{t_0+\Delta t} \\ \ddot{\rho}^{t_0+\Delta t} \end{bmatrix}^T = \hat{f}_{\rho, \text{Newmark}}(X_{\rho}^{t_0}, \Delta t, \Delta \hat{\rho}^{t_0+\Delta t}) = \begin{bmatrix} \rho^{t_0} + \dot{\rho}^{t_0} \Delta t + \ddot{\rho}^{t_0} \frac{\Delta t^2}{2} + \Delta \hat{\rho}^{t_0+\Delta t} \frac{\Delta t^2}{4} \\ \dot{\rho}^{t_0} + \ddot{\rho}^{t_0} \Delta t + \Delta \hat{\rho}^{t_0+\Delta t} \frac{\Delta t}{2} \\ \ddot{\rho}^{t_0} + \Delta \hat{\rho}^{t_0+\Delta t} \end{bmatrix}^T,$$

where the second order perturbation is expressed by the following dot product:

$$\Delta \hat{\rho}^{t_0+\Delta t} = \begin{bmatrix} \frac{\hat{q}_{\rho}^{t_0+\Delta t} \omega \tan(\Delta \varphi)}{\Delta t} & -\frac{1}{\Delta t} & -1 \end{bmatrix} \begin{bmatrix} \rho^{t_0} \\ \dot{\rho}^{t_0} \\ \ddot{\rho}^{t_0} \end{bmatrix}$$

For further details on the theory behind these expressions see (Brochner & Macías, 2014).

- **Graphical representations**

Graphical representations of flow vectors for the sub-cluster flow are based on the global reference frame. The transformations from local cylindrical coordinates into global Cartesian coordinates are:

$$\text{Position: } \begin{bmatrix} r_X^{t_0+\Delta t} \\ r_Y^{t_0+\Delta t} \\ r_Z^{t_0+\Delta t} \end{bmatrix} = \begin{bmatrix} \cos(\varphi) \rho^{t_0+\Delta t} \\ \sin(\varphi) \rho^{t_0+\Delta t} \\ z \end{bmatrix}$$

$$\text{Velocity: } \begin{bmatrix} v_X^{t_0+\Delta t} \\ v_Y^{t_0+\Delta t} \\ v_Z^{t_0+\Delta t} \end{bmatrix} = \Theta \begin{bmatrix} \dot{\rho}^{t_0+\Delta t} \\ \omega \rho^{t_0+\Delta t} \\ z \end{bmatrix}^T$$

$$\text{Acceleration: } \begin{bmatrix} a_X^{t_0+\Delta t} \\ a_Y^{t_0+\Delta t} \\ a_Z^{t_0+\Delta t} \end{bmatrix} = \Theta \begin{bmatrix} \ddot{\rho}^{t_0+\Delta t} - \rho^{t_0+\Delta t} \omega^2 \\ 2\dot{\rho}^{t_0+\Delta t} \omega \\ z \end{bmatrix}^T$$

where Θ is the rotational matrix.

$$\Theta = \begin{bmatrix} \cos(\varphi) & -\sin(\varphi) & 0 \\ \sin(\varphi) & \cos(\varphi) & 0 \\ 0 & 0 & 1 \end{bmatrix}$$

2.2. Data acquisition from high speed videos

In order to visualize the behaviour of the sub-cluster, videos of the spinning disk spreading salt are collected using a modular and compact high speed camera suitable for research applications. There are several different possible approaches. Basically, the

camera could focus perpendicularly on the disk (B), in parallel on the disk (C) or it could just look at the disk with some angle of inclination (A) as it is shown in Figure 17. As there was only one high speed camera available for this research, the configuration chosen was the (A). This configuration is expected to provide data about the salt along the $\rho\phi$ -plane and the ρz -plane.

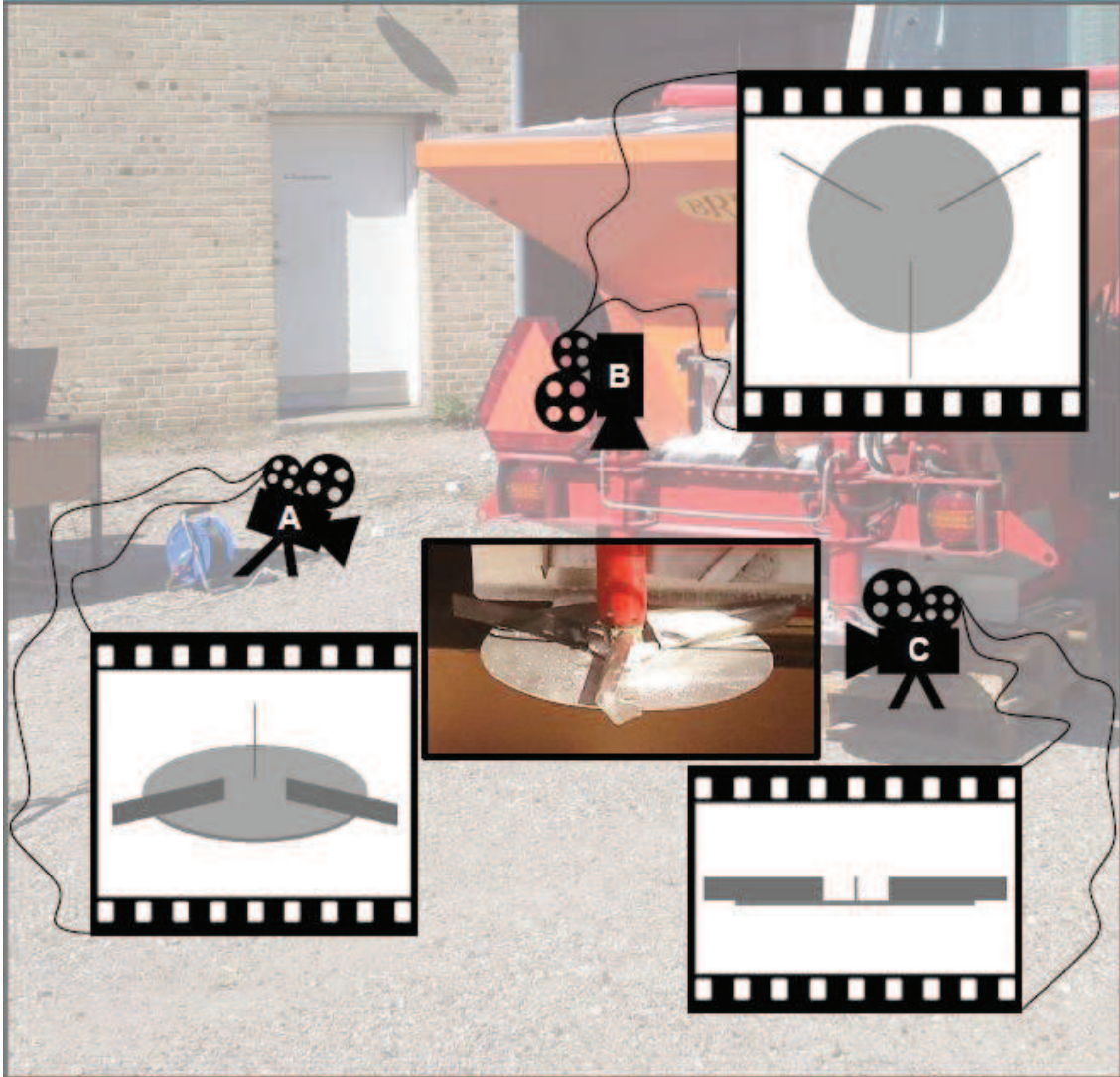


Figure 17. Camera dispositions

2.2.1. Plane projections

The frames obtained from this camera configuration (A) show perspective views of the salt evolution on the blade, therefore measurements could not be taken directly from these images because they provide deformed reality.

In order to obtain the real lineal and angular magnitudes of the salt, disk and blades, the plane which contains these elements is placed in parallel or contained in the horizontal plane of projection. Thus, the projections are shown in real magnitude on the plane of projection corresponding since, if the surface to project and the plane of projection are parallel or coinciding there are not lineal or angular deformations in the figure projected.

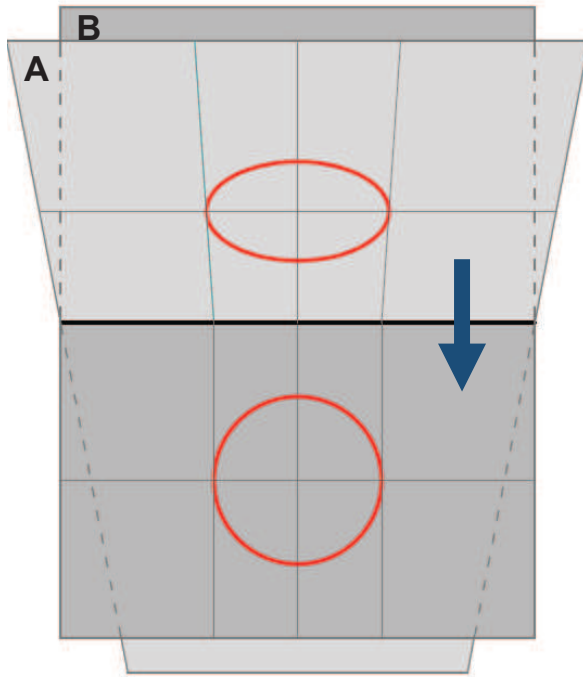


Figure 18. Projection of disk's edge on both planes

Project the plane **A** onto the plane **B** means to make them coincide using the line intersection between them as a hinge (Figure 18).

This trick allows us to measure every magnitude needed from the $\rho\varphi$ -plane (base of the triangle, see section 2.2.2.).

The measurements in the ρz -plane are performed by simple proportion knowing the height of the blade along the vane, 5 cm. In this case, the measured magnitude is along a line contained in the same plane, it means there is no need to any further consideration (high of the triangle, see section 2.2.2.)

Figure 19 shows an example of how to find some points of the perspective view (plane A) on the horizontal plane (plane B). The pink line is a representation of the perimeter of vane in contact with the disk. The points 1-2 and their projections 1'-2' illustrate how to get a perpendicular segment in any point of the vane to can measure along them the dimensions from the $\rho\varphi$ -plane.

In this particular view it is show the relation between the real dimension of the blade (28,1cm) and the one measured directly from the perspective view (24,5cm). The same way, any distance needed for calculations was obtained.

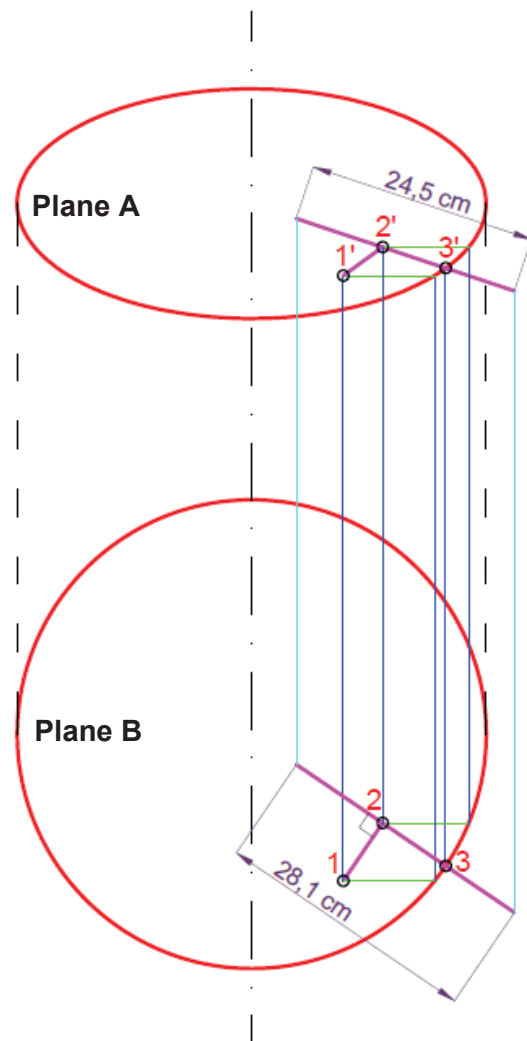


Figure 19. Relation between measurements on both planes

2.2.2. Considerations taken to obtain radial velocity data

As it was suggested in section 2.1.3., radial velocity and transversal area of salt of each sub-domain are related. This relation can be specified through the following expression:

$$\dot{m} = \frac{dm}{dt} = \frac{\rho_{\Omega} V_{\Omega}}{dt} = \frac{\rho_{\Omega} A_{\Omega} \Delta\rho}{dt} = \rho_{\Omega} A_{\Omega} \dot{\rho} \rightarrow \dot{\rho} = \frac{\dot{m}}{\rho_{\Omega} A_{\Omega}}$$

where, a sub-cluster of particles has been discretized underway into finite sub-domains Ω with length $\Delta\rho$. Therefore, to obtain the value of the radial velocity $\dot{\rho}$, the value of the mass flow \dot{m} is needed. Also necessary are the area A_{Ω} and the empiric density ρ_{Ω} of each sub-domain along the radial axis considered (Figure 20).

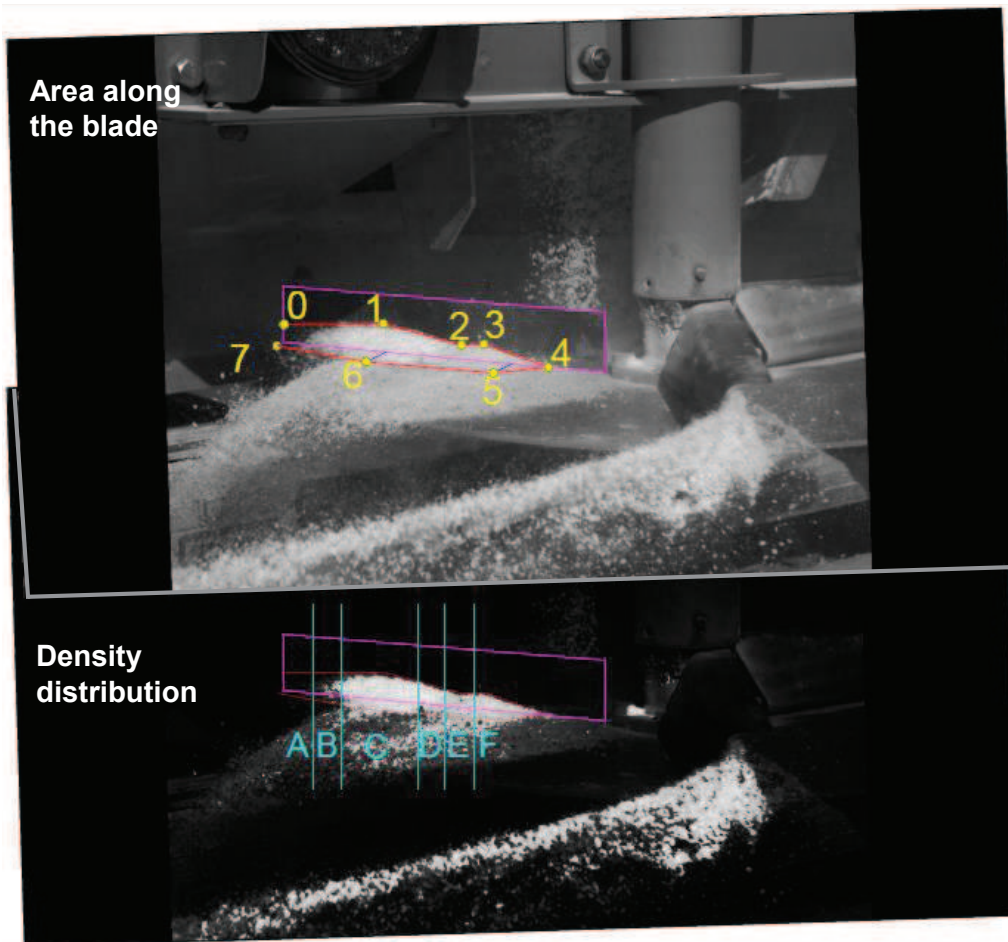


Figure 20. Identification of area and density sections

- **First step: frame selection**

The spreader disk has been recorded spreading salt under five different rotation speeds. Each of these videos includes the system movement along two seconds. In this time, the disk gives several turns (the exact number depends on the rotation speed). The search of the radial scale parameter is based on the study of one particular frame of these videos for each disk velocity ergo it is extremely important to select the appropriate image in every case.

In Figure 21 it is shown a frame extracted from a high speed video and in parallel it is highlighted the existing relation between radial velocity and sub-domain areas. The adequacy of the image resides in the situation of the blade at the moment taken. The straight blade has just left the inflow zone, when only a few percentage of the salt dropped has already left the disk and most of the salt has already been collected by the vane.

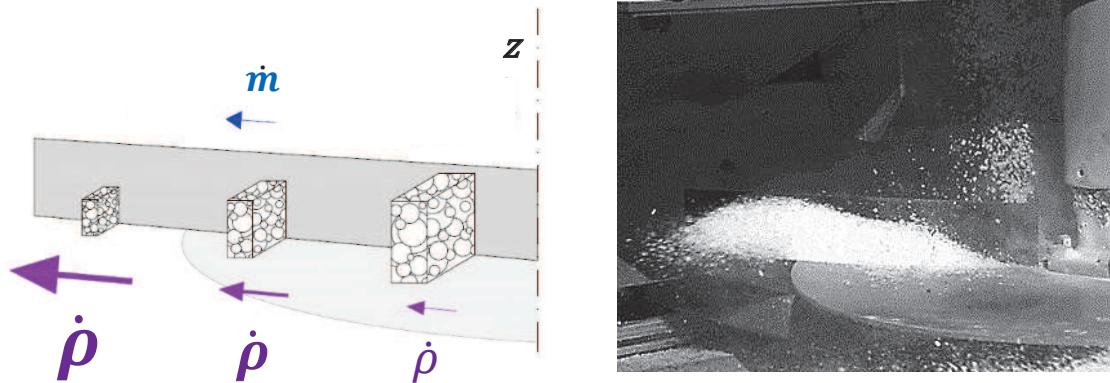


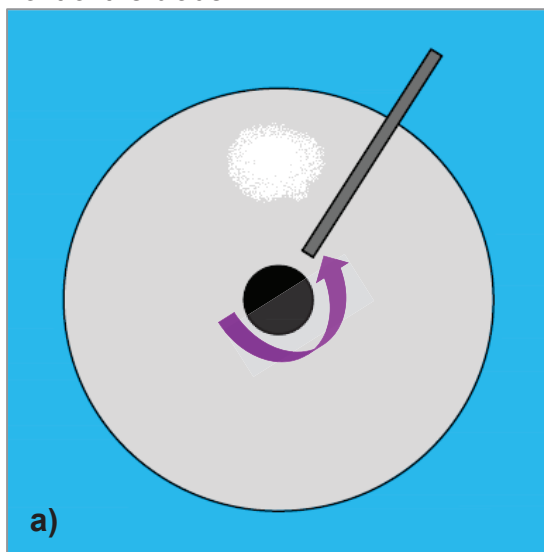
Figure 21. Distribution of salt along the blade in a particular frame

- **Second step: obtention of the mass flow value**

Assuming a constant flow, the data needed were obtained weighting the amount of salt dropped on the disk in certain periods of time. Details about the mass flow calculations are explain in chapter 3: results.

Before including the obtained value of mass flow (0,974 kg/s) in the calculations of the radial velocity, some further considerations must be taken into account. In Figure 22 it is illustrated the sub-cluster flow of particles since the moment they are dropped down (a) until the moment the blade reaches the position of the frame studied (b).

Inflow. Particles are dropped down in front of the blade.



Underway. Particles are collected by the blade.

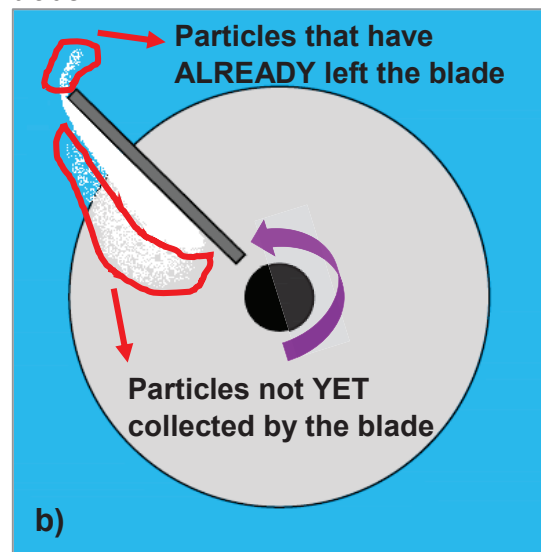


Figure 22. Salt particles flow

There is a percentage of the salt not gathered by the blade at the instant the frame is taken. This fact is considered in calculations by applying a reduction, in the form of a percentage, to the mass flow. As it is detailed in Annex 6.1., every spreader disk velocity is corresponded to a percentage based on observation of the fraction of salt collected and not by the vane in the frame analysed.

- **Third step: calculation of the area of each sub-domain in the chosen frame**

Situating the high speed camera levelled with the disk, as in Figure 23a, it is appreciated a triangular shape sub-cluster when the salt is collected by the blade. The same geometry is present in different sizes along the vane (Figure 22b) and is caused by the movement of the spreader disk gathering the salt towards the vane and the gravity.

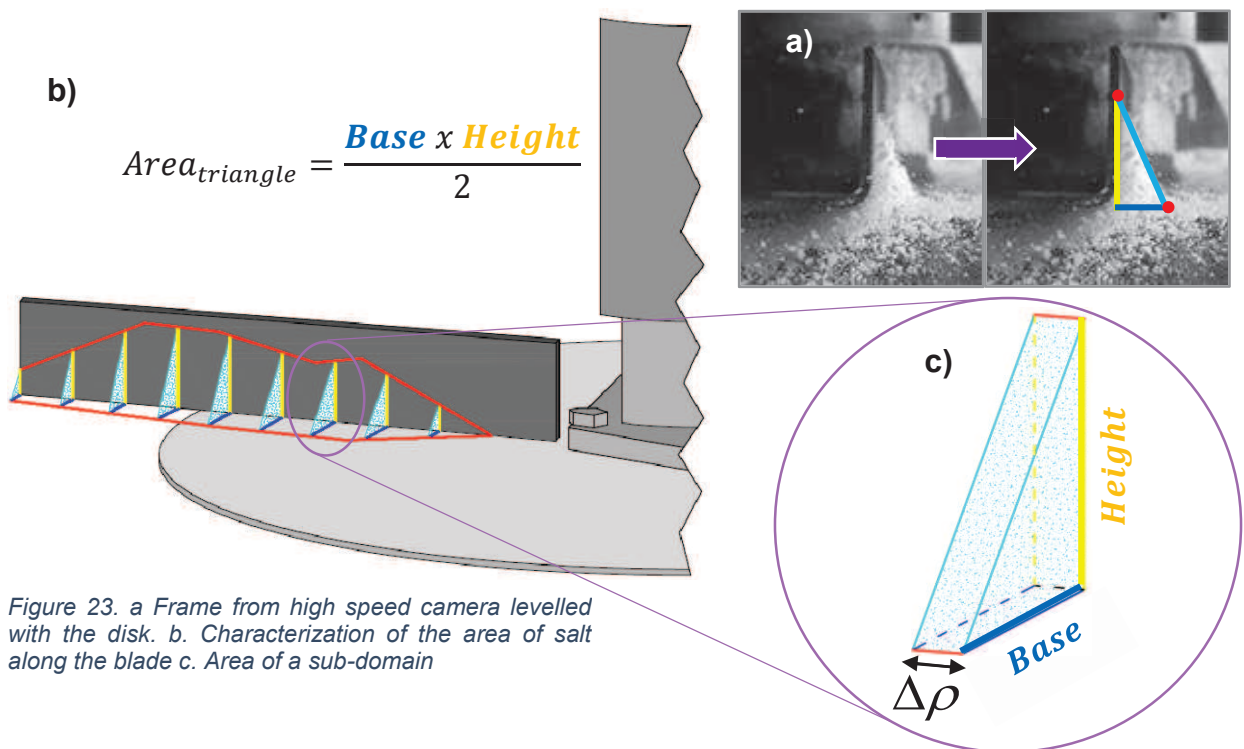


Figure 23. a Frame from high speed camera levelled with the disk. b. Characterization of the area of salt along the blade c. Area of a sub-domain

The areas of such triangular sub-domains are obtained by defining the piecewise linear lines (red) along the blade (Figure 24). To this end, first the coordinates of the points highlighted are determined and then the equations of the lines joining them calculated.

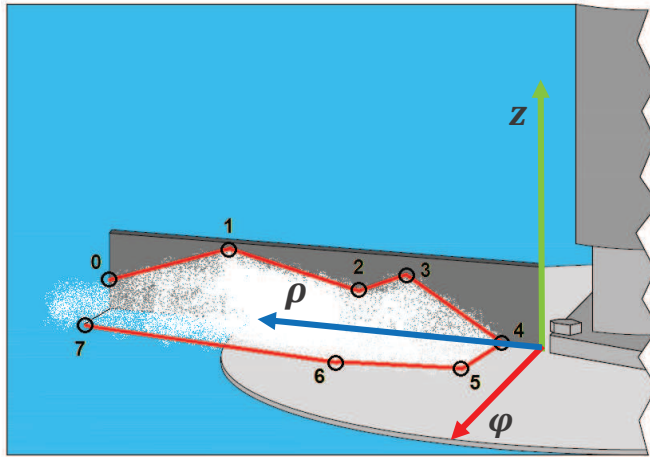


Figure 24. Coordinates of the required points

The equation of a straight line with gradient m and intercept c on the $z\rho$ -plane is defined as:
 $z = m\rho + c$

Where, as it is shown in Figure 23, z provides the height of every sub-domain along the ρ axis.

With the aim of finding the base of the triangle, the red lines joining the points 4-5, 5-6 and 6-7 are characterized, in the $\rho\phi$ -plane, as: $\phi = m\rho + c$

Annex 6.1. covers in detail the calculation of the area for each speed.

- **Fourth step: estimations of the empiric density of each sub-domain of the sub-cluster in the specific frame**

A coefficient of compaction C_c is defined in order to normalize relative to solid salt.

$$C_c = \frac{\rho_\Omega}{\rho_c}$$

Where C_c goes from 0 (not salt at all) till 1 (solid fraction).

The solid salt density ρ_c is considered to be 2165 kg/m³ (Weast & Astle, 1981-1982).

Therefore, the coefficients of compaction for each one of the sections must be defined.

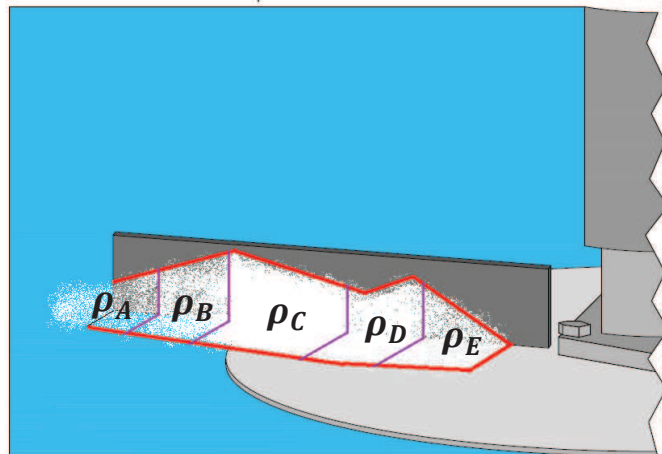


Figure 25. Distinction of sections with different densities

Figure 26 exemplifies this variation from a single frame, from a high speed video, where changes in levels of contrast and brightness reveal the variations in the salt densities and an approximated subdivision into sections with different concentration of salt that are fitted by piecewise linear boundaries is illustrated in Figure 25.



Figure 26. Appreciation of density distribution

Further details on the subdivision of sections and coefficients of compaction for the various rotation speeds are provided in Annex 6.1.

- **Last step: obtaining results**

Once the values of mass flow, density and area (defined above) have been obtained for every radial position along the vane, is time to apply the expression highlighted at the beginning of this chapter:

$$\dot{\rho} = \frac{\dot{m}}{\rho_{\Omega} A_{\Omega}}$$

MATLAB® algorithm has been developed for the determination of values for the radial velocity of each sub-domain along the vane in a certain time instant. An example of results from this novel algorithm is shown in Figure 27 in a graphic way with the radial position ρ as abscissa as the radial velocity $\dot{\rho}$ as ordinate. The graph clearly indicates two significant zones. One zone is called the “adjustment phase”. In this zone the radial velocity decreases sharply and a section where the radial velocity grows exponential. Henceforth, the “adjustment phase” is neglected for approximation since it represents a zone where the particles in front of the vane are messy. In the “exponential tendency” phase the particles are observed to find their place on the vane.

At the particular moment immortalized for the frame from the high speed camera, the model for each disk rotation speed analysed, is obtained by fitting the data of the “exponential tendency” section to a mathematical function. The intention is to capture important patterns in the evolution of the radial velocity while leaving out noise.

The fitting has been carried out using the MATLAB® Curve fitting tool. This tool has done the process of finding the mathematical function which best fits to a series of radial velocity data points for each radial position.

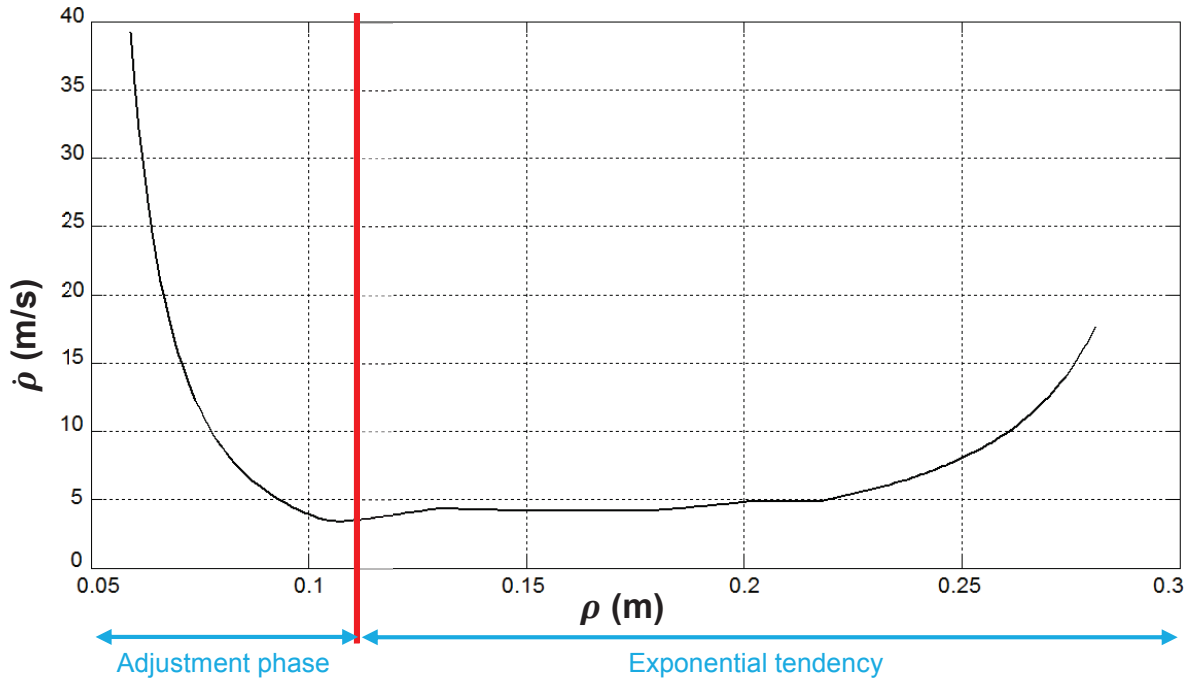


Figure 27. Sections in the radial velocity data

An approximating function of the form $\dot{\rho} = a \cdot e^{b \cdot \rho} + c$ is used for all fittings presented in the Annex 6.2. The three fitting parameters a, b & c can be determined from a standard curve fitting tool.

Where, the parameter a is called the function's ordinate-intercept, b is the constant rate and c represents the vertical translation of the data in an exponential function with base e.

Figure 28 shows an example of radial velocity data, in black, fit with the exponential function mentioned, in blue.

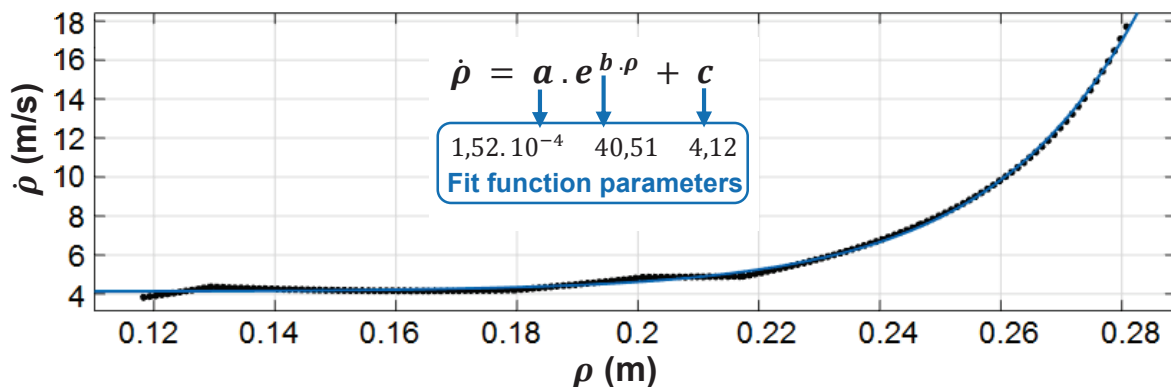


Figure 28. Fit of the data with a three parameters exponential function

After fitting data with the exponential function $\dot{\rho} = a \cdot e^{b \cdot \rho} + c$, the goodness of fit is evaluated. The first step is a visual examination of the fitted curve displayed what allows to visualise the entire data set at once. Beyond this, the MATLAB® Curve fitting tool also

provides numerical methods to determine goodness of fit. The toolbox provides for separate goodness of fit statistics²:

- Sum of Squares Due to Error (SSE)

This statistic measures the discrepancy between the data and the estimation model.

$$SSE = \sum_{i=1}^n \omega_i (y_i - \hat{y}_i)^2$$

where, n is the number of observations, ω_i is the weighting applied to each data point, y_i is the observed data value and \hat{y}_i is the predicted value from the fit.

The fit is more useful for prediction when the SSE value is closer to 0.

- R-Square

This coefficient determines the quality of the model to replicate the results, and the proportion of variation in results that can be explained by the model. R-square is defined as the ratio of the sum of squares of the regression (SSR) and the total sum of squares (SST).

$$SSR = \sum_{i=1}^n \omega_i (\hat{y}_i - \bar{y})^2$$

$$SST = \sum_{i=1}^n \omega_i (y_i - \bar{y})^2$$

$$R - square = \frac{SSR}{SST} = 1 - \frac{SSE}{SST}$$

where $SST = SSR + SSE$ and \bar{y} is the mean of the observed data

The value of R-square ranges between 0 and 1. A value closer to 1 indicates that a greater proportion of variance is explained by the model.

- Degrees of Freedom Adjusted R-Square

This coefficient uses the R-square statistic defined above and incorporates the model's residual degrees of freedom. It is interpreted as the proportion of total variance that is explained by the model. The residual degrees of freedom is defined as the subtraction between the number of response values n and the number of fitted coefficients m calculated from the response values.

$$v = n - m$$

where v defines the number of pieces of independent information involving the n data points that are needed to calculate the sum of squares.

$$adjusted\ R - square = 1 - \frac{SSE(n - 1)}{SST(v)}$$

² For more details see: <http://www.mathworks.se/help/curvefit/evaluating-goodness-of-fit.html>

The adjusted R-square coefficient can be any value less than or equal to 1. The fit is better when the value is closer to 1.

- Root Mean Squared Error

It is an estimation of the standard deviation of the differences between predicted values and observed values.

$$RMSE = s = \sqrt{MSE}$$

where MSE is the mean square error

$$MSE = \frac{SSE}{v}$$

The fit is more useful for prediction when the MSE value is closer to 0.

In order to analyse the goodness of fit of the models, a combination of the four coefficient described above has been used. For further details see Annex 6.2. where a complete description of the process followed for some distinct rotation speeds of the disk studied is presented.

3. Results

3.1. Introduction to results

The goal is to visualize in reality the behaviour of a sub-cluster of salt particles on the spreader disk. Ad hoc, movies of the spreader disk running and spreading salt were shot using a high speed camera. Following, in the Figure 29, it is shown one example of layouts used to take the shoots outdoors and the equipment needed. Throughout filming, the tractor was steady and the only movement came from the salt spreader unit, attached to the tractor.

The analysis of the images from the high speed camera, as highlighted in section 2.2.2., required to know the value of the mass flow for each setting of the salt spreader unit. These measures were obtained indoors in order to avoid, as far as possible, imprecisions due to environmental factors. All equipment needed was a box, a timer and a balance.

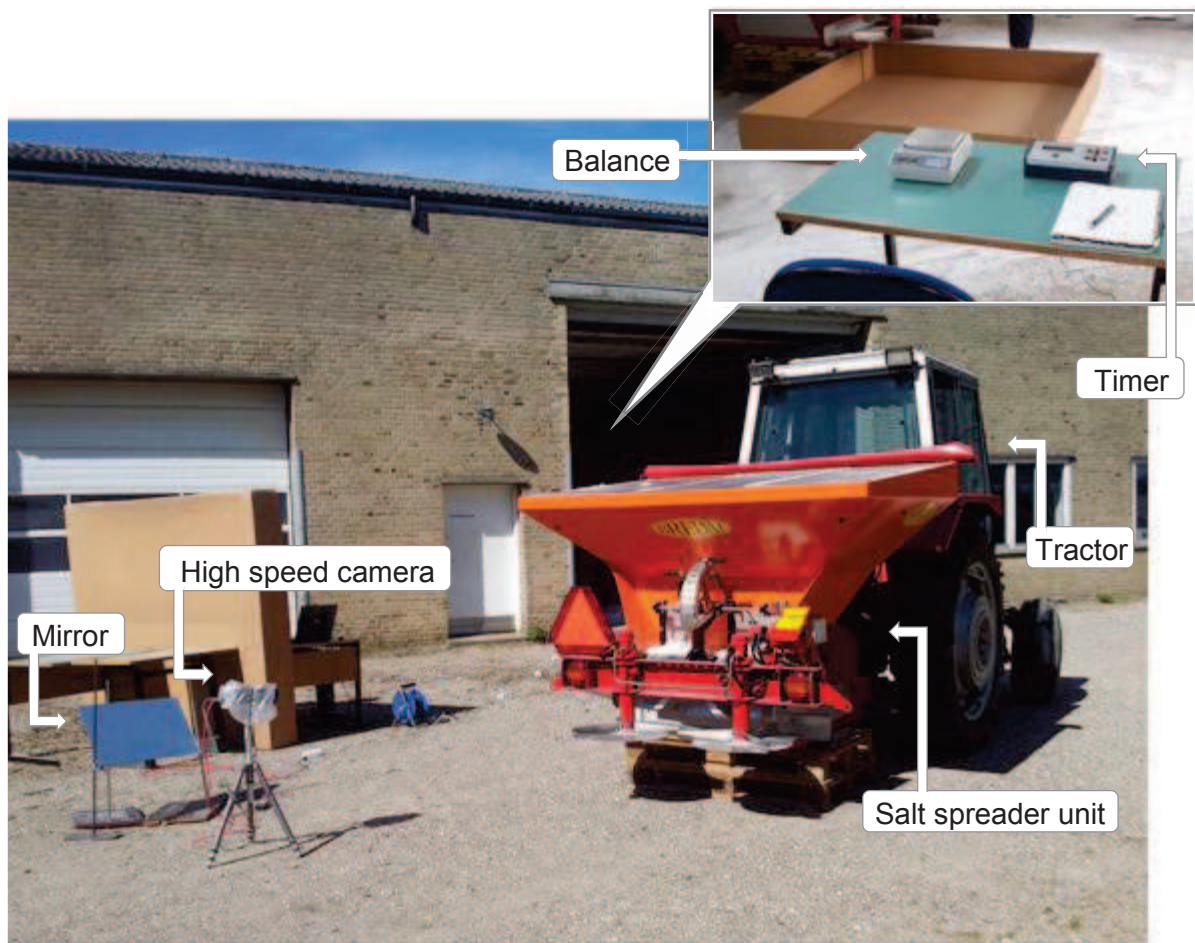


Figure 29. Film set

Limitations in the lighting equipment available forced the shoots to be taken outdoors in daytime. Therefore, the sun has been the main and unique light source. A different setting was used for practically every shooting made because of the changing nature of the environmental weather. Besides, a mirror was used to concentrate sun light in the right position on the straight blade avoiding shades in critical places. In short, the lighting condition in every filming session highly influenced the quality of the images obtained.

Depending on the weather had many drawbacks, the timing of shooting sessions became crucial to avoid wind, clouds and unsuitable sun positions.

3.2. Equipment and data processing

3.2.1. Tractor

The role of the tractor in this research is not really important since it only provides hydraulic power to the salt spreader unit which is controlled by the spreader control system.

- Model: Massey Ferguson 675 SU
- Serial no.: K320006
- Engine no.: U930800

3.2.2. Salt spreader unit

This unit is powered by the tractor and connected to its back. The tractor's hydraulic motors are in charge of the two spinning disks' rotation. The velocity of the disk and the flow of salt are governed by a control system placed in the cabin of the tractor.

- Manufacturer: Bredal A/S Denmark
- Model: SGS1500
- Manufacturing year: 2012
- Net weight: 450 kg
- Total weight: 2000 kg

The salt spreader unit is composed of:

- Spreader disks

Even though there are two spreader disks in the salt spreader unit, for this research only one was used.

Originally this spreader disk was equipped with three identical U-shape blades but, in order to fit the reality with the mathematical model, one of these U-shape blades was replaced with an L-shape beam.

Within the scope of this dissertation only matters the behaviour of the salt on this straight vane installed. Therefore, the images taken are all destined to understand the salt flow occasioned by the straight blade. Future research will be developed for studying more complex vane geometries.



Figure 30. Spreader disk used

Table 1. Salt spreader disk remarkable characteristics

Vane	
Length	281 mm
Height	50 mm
Thickness	3 mm
Starting point on the disk	64 mm from the centre

Disk	
Diameter	500 mm

- A spreader control system

The salt flow is commanded complementarily by a control panel managed from the tractor seat and a rear gate situated in the back of the salt spreader unit. The first gadget controls the belt speed and the velocity of the disk. The second accessory adjusts manually the amount of salt dragged by the belt. As a result, the mass flow of salt leaving the spreader unit is function of both devices.



Figure 31. Computer setting



Figure 32. Manual setting

Settings for the experiments made:

Table 2. Experimental settings for the spreader unit

Application rate setting	
Grams/m ²	115 g/m ²
Width (m)	15.0 m
Specific gravity	1.41
Step %	10
Scale position	20
Flow factor	1.00

Additional setting	
Speed simulate	40 km/h
Manual setting of flow	30

3.2.3. High speed camera

The frames of the spinning disk spreading salt are collected using a modular and compact high speed camera suitable for research applications.

- Model: AOS S-PRI plus 2124
- Technical data:



Figure 33. High speed camera

Table 3. High speed camera features

Technical key specifications	
Sensor (type, resolution)	Progressive CMOS, 900x700 pixels, mono or colour (1280 x 1024 pixels with option 2)
Sensor size	12,6 x 9,8 mm (@ 900 x 700), 14 µm pixel size
Light sensitivity	ISO 3200 (monochrome), ISO 1600 (colour)
Frame rate at full resolution	Up to 1'000 fps @ 900 x 700 pixels
Max. frame rate	1'250 fps (max. 16'500 fps with option 3)
Image memory	Built-in DRAM, circular buffer
Sequence length (typical)	2,1 s @ 900 x 700/1'000 fps (1,3 GB memory) 4,2 s @ 900 x 700/1'000 fps (2,6 GB memory) 8,4 s @ 900 x 700/1'000 fps (5,2 GB memory) 16,9 s @ 900 x 700/1'000 fps (10,4 GB memory)
Power supply	12 VCD (9...16VDC)
Power consumption	15 W (w/o data link), 18 W (with data link)
Built-in battery, capacity	NiMH, 30 minutes
Data Interface	Gigabit Ethernet (1'000 Mb/s) RMS, other connectors on request
Size, weight	72 x 72 x 122 mm, 900 g

Options	
Option 1	Gain control (5-,8- or 10 bit, low-, mid- or high gain)
Option 2	Full resolution (1280 x 1024)
Option 3 PRI	Extended speed (16'500 fps)

Option 4	3 additional event markers (total of 4)
Option 5	Frame synchronization, multi camera operation
Option 11	Auto Exposure
Option 12	Motion Detection

3.2.4. Balance

The devices available in the salt spreader unit facilitate to change the amount of salt leaving the system but they do not give accurate information about the mass flow data. This quantity will be needed for calculations hence its value is determined using a precision balance.

- Model: KERN 440-35A



Figure 34. Balance KERN 440-35A

- Technical data:

Table 4. Balance features

Weighing range [Max]	Readout	Reproducibility	Linearity	Min. piece weight	Weighing plate [ø]
600 g	0,01 g	0,01 g	± 0,03 g	0,02 g	105 mm

3.2.5. Timer

Complementary to the balance a timer is needed in order to get the mass flow. The chosen unit incorporates more features than really needed. It could perform measurements using microphones, free-fall equipment and other mechanical or electronic switches. For this first approach was enough with activating the timer manually losing accuracy but still getting a significant value.

- Model: Student timer 2002.60



Figure 35. Timer 2002.60

- Technical data:

Table 5. Timer characteristics

Display	Resolution	Max. counting time	Batteries	Power adapter
5 digit LED	0.01 ms	99999 s	3510.06 (6 ea.)	3550.15

3.2.6. Mirror

A conventional mirror with dimensions of 385x585 mm is used to concentrate sun light on interesting parts of the vane getting better images and avoiding shadows.

3.3. Flow measurements and considerations

With the salt spreader unit set according to section 3.2.2., three combinations of weight and time were taken and the mass flow calculated for each one (Table 6).

Table 6. Mass flow measurements

	Salt mass (kg)	Time (s)	Flow mass (kg/s)
Data collection 1	17,405	17,4	0,999
Data collection 2	15,671	16,2	0,968
Data collection 3	16,400	17,2	0,955

The mean (or average) of these three measurements: $\dot{m} = 0,974 \text{ kg/s}$

In order to indicate how representative this average is, a measure of dispersion consisting in subtracting the lowest mass flow data measured to the highest and divide that between the average, can be presented: $\%D = 4,52\%$

Taking into account the limitations in the equipment highlighted along sections 3.1. and 3.2., a value under 5% is acceptable (Villasuso, 2003). Thus, the average is considered as representative and there is no need to take more measurements.



Figure 36. Measurement of mass flow in progress

3.4. Radial scaling functions

Following the detailed instructions of chapter 2.2.2., the radial velocity data obtained from processing frames from high speed videos are fitted to an approximating function defined by three fitting parameters a , b & c and an exponential term.

As already mentioned, the fit function is of the form: $f_i(\rho) = a_i \cdot e^{b_i \cdot x} + c_i$ and the fitting parameters are obtained using the MATLAB® Curve fitting tool.

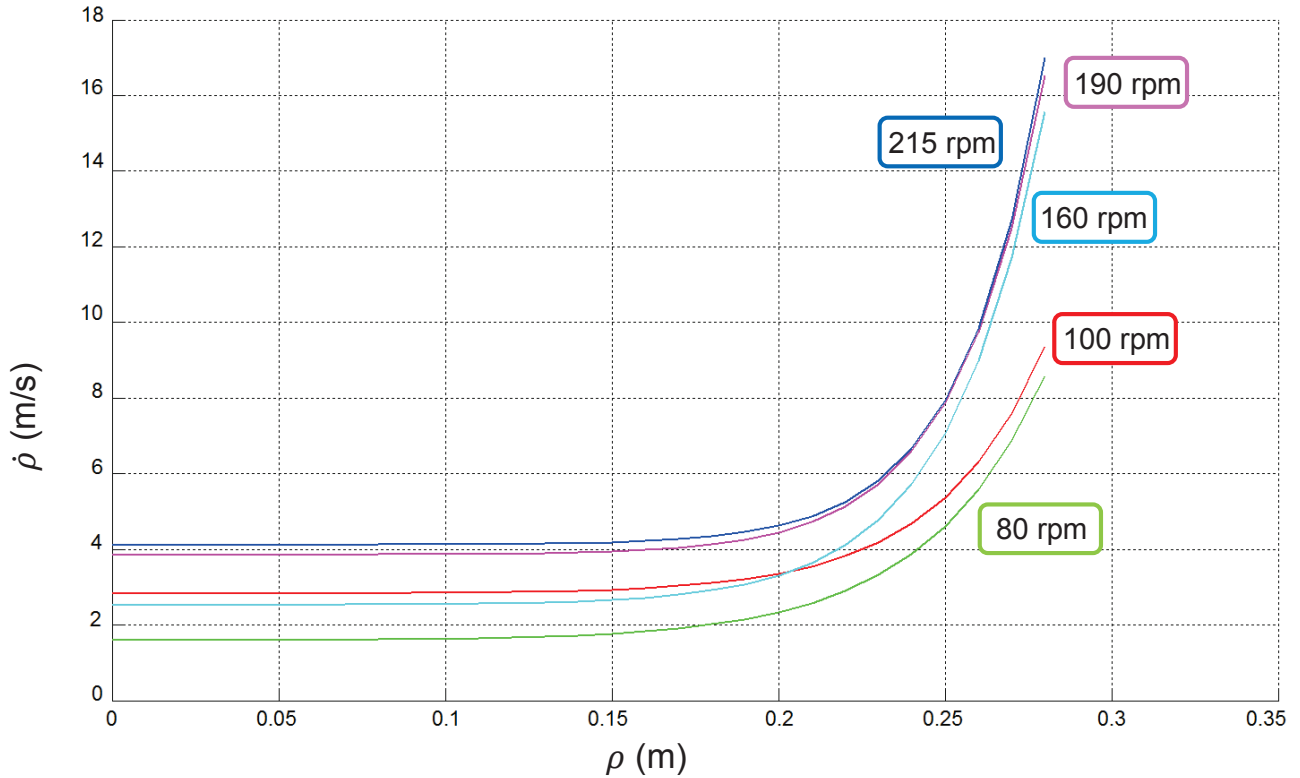


Figure 37. Radial velocity representation along the vane

Figure 37 shows the graphical representations of these 5 approximate functions along the radial position at a characteristic instant of time.

Table 7. Collection of fit function parameters and calculation of radial velocities at the edge of the disk

i	Disk rotation speed (rpm)	Coefficients of the exponential function			Radial velocity of the sub-domain leaving the disk (m/s)
		a	b	c	
1	80	$2,757 \cdot 10^{-3}$	27,94	1,560	8,64
2	100	$9,625 \cdot 10^{-4}$	31,45	2,782	9,41
3	160	$6,820 \cdot 10^{-4}$	35,15	2,486	15,77
4	190	$2,783 \cdot 10^{-4}$	38,25	3,794	16,75
5	215	$1,503 \cdot 10^{-4}$	40,51	4,051	17,25

Table 7 collects the fitting parameters determined by using MATLAB® Curve fitting tool and the value of the radial velocity in the edge of the vane for every disk rotation speed.

The goodness of fit of these approximate functions is evaluated through a combination of goodness of fit coefficients also provided by MATLAB®. In general good agreement is achieved as seen in Table 8.

Table 8. Summary of the goodness of fit coefficients evaluated

Disk rotation speed (rpm)	Goodness of fit			
	SSE	R-square	Adjusted R-square	RMSE
80	0,2055	0,9993	0,9993	0,04651
100	0,8359	0,9968	0,9967	0,09637
160	2,109	0,9988	0,9988	0,1104
190	17,99	0,9885	0,9883	0,3272
215	2,084	0,9987	0,9986	0,1127

The SSE and RMSE coefficients corresponding to the rotation velocity of 190 rpm are out of the overall tendency. This means, the model values are not as close as in the other velocities to the observed data points. It can be noticed visually, in Annex 6.2., how the radial velocity data present a sharp drop around position 0,2m along the vane. In the following the two data set with outliers for the SSE and RMSE are not included. Therefore, only for this reduced data set (where these two values are discarded), the coefficients of the goodness of fit for the different rotation speeds are included in the following intervals:

$SSE \in [0,2055 - 2,109]$ Values close to 0 mean data and model's predicted values are not so far.

$R - square \in [0,9885 - 0,9993]$ Values close to 1 mean the model success in explaining the variation of the data.

$Adjusted R - square \in [0,9883 - 0,9993]$ Values close to 1 mean it is a good fit.

$RMSE \in [0,04651 - 0,1127]$ Values close to 0 mean observed data points and model's predicted values are close.

4. Discussion

4.1. Perspectives and un-answered questions

In this first study, a series of assumptions and approximations were made.

The novel kinematic shape functions intend to incorporate the non-stationary flow complexities due to sliding, rolling and repositioning of the particles inside the salt sub-cluster. That means that the approach includes, at least in a mean value approach, the effects from impulsive forces and moments.

The definition of the radial scaling function, which is the key focus for this work, needs the identification of different density sections and their coefficients of compaction along the vane at a characteristic instant of time. This task, in this first approach, was developed by simple observation.

It is likely, that an improved and extended experimental setup would increase the quality of the high speed videos in respect to contrast and focus and the number of angles for recording. This means that an even more refined model which improves its ability to predict the motion of the sub-cluster along the vane could be developed.

Limitations were also found in the equipment and data processing. The high speed videos were filmed focusing on a spreader disk, originally equipped with three curved vanes. One of these blades was exchanged by the straight blade focus of this study. The differences in geometry and weight between the two types of blades installed on the disk caused vibrations and decompensations in the system while the disk was spinning spreading salt. For future research is highly recommended to match all the blades of the disk.

The geometry of the spreader unit itself hinders the filming of the spreading process from some interesting angles, such as top view. As this study is only focused on the kinematics of the sub-cluster on the disk, a future experimental setup might be designed to isolate the spreader disk from the unit and thereby enable filming with the high speed camera from any angle.

The high speed camera needs plenty of light to get good images. Limitations in the lighting equipment available forced us to record the movies outside, what means the wind could introduce some noise in the data collection.

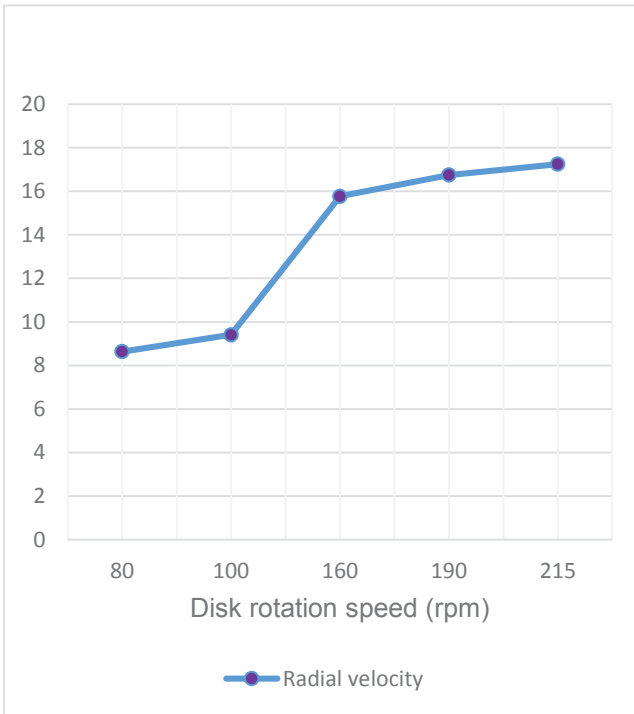


Figure 38. Radial velocity of sub-domains leaving the disk

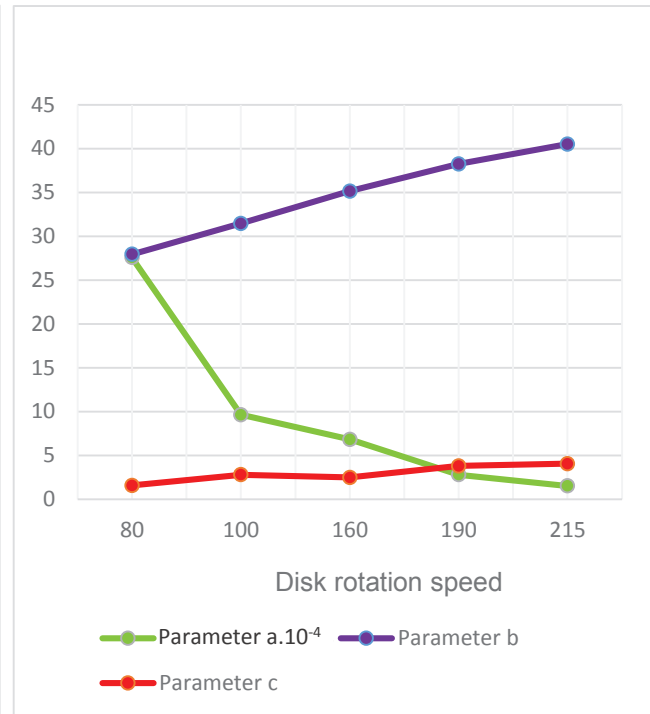


Figure 39. Fit function parameters

The radial velocity data obtained from the high speed videos were fitted using exponential functions of the form: $\dot{\rho} = a \cdot e^{b \cdot \rho} + c$. The fitting was carried out using the MATLAB® Curve fitting tool. Figures 38 and 39 show the values of the three parameters of the fit functions and the respective radial velocity of the sub-domain leaving the disk. The analysis of the numerical methods to determine goodness of fit, also provided for the MATLAB® tool mentioned above, shows that there not significant differences between observed kinematic values and the fitted values. Even though there is no relation established yet between these parameters obtained, the graphs show a clear tendency and existing relation between their values for the different rotation speeds. While the parameter a decrease with the rotation speed, the rest of the parameters increase as the rotation speed goes up. Overall, these findings support the hypothesis that this novel model for radial kinematics can fit real world observations through a shape function with only three parameters. Also this piloting study shows that further research in this area could led to a significant knowledge bank of experimental data based on high speed videos for various vane designs that could be used to simulate the outflow properties for new designs. Such simulations will cut down development cost and reduce the development and the testing phase for manufacturers of salt spreader units.

4.2. Conclusion

Although, the data of radial velocities of the rock salt for the disk and blade configurations used in this study is not found in other research, the kinematic results can be compared to other works. Disk dimensions and vane geometries are not the same in comparable studies; however the range of radial velocities obtained in the edge of the disk is in

agreement with several authors (Takai, 2013; Van Liederkerke et. al, 2009; Van Liederkerke et. al, 2006).

The key finding of this study is that a novel model for the radial kinematics, based on the development of a radial scaling function with only three parameters is able to fit real world observations. This means a novel software that can predict the radial velocity outflow for arbitrary rotation speeds can be developed on the top of this study. Furthermore, when more experiments with different vane designs are performed such novel software would also be able to predict the outflow from new cutting edge designs of the future.

This piloting study is based on a simplified model; however its promising results encourage to extended studies on stochastic sub-cluster kinematics for spreader disks in close collaboration with manufacturers. Ultimately, future spreader disks are to be developed by new tools that might lead to more efficient spreader designs that minimize cost related to salt spreading and reduce negative impacts on the nature.

5. References

5.1. Literature

- AGREX S.p.A 2014. *Productos*. [Online] Available at: <http://www.agrex.it/> [Accessed 05 May 2014].
- Agriaffaires 2014. *Farming*. [Online] Available at: <http://www.agriaffaires.co.uk/> [Accessed 05 May 2014].
- Aphale, A., Bolander, N., Park, J., Shaw, L., Svec, J. & Wassgren, C. 2003, "Granular Fertiliser Particle Dynamics on and off a Spinner Spreader", *Biosystems Engineering*, vol. 85, no. 3, pp. 319-329.
- BOGBALLE A/S 2014. *Salt spreaders*. [Online] Available at: <http://www.bogballe.com/> [Accessed 05 May 2014].
- BREDAL A/S 2014. *Products*. [Online] Available at: <http://www.bredal.com/en/home> [Accessed 05 May 2014].
- Brøchner, T. 2013. Natural Parameterization. Department of Engineering. Aarhus University. Denmark. 252 pp – Technical report ME-TR-5.
- Brøchner, T. & Macias, P. 2014, "Report 15: Parameterized Kinematics of Salt Particle Movements on a Spinning Spreader Disk ", Research for Building, Energy and Environment, VIA University College (In process).
- Cointault, F., Sarrazin, P. & Paindavoine, M. 2002, "High resolution low cost imaging system for particle projection analysis: Application to fertilizer centrifugal spreading", *Measurement Science and Technology*, vol. 13, no. 7, pp. 1087-1093.
- Cundall, P.A., 1971, "A computer model for simulating progressive large-scale movements in block rock mechanics", *Proc. Symp. Int. Soc. Rock Mech. Nancy*, p. 2.
- Cunningham, F.M. 1963, "Performance characteristics of bulk distributors for granular fertilizer", *TRANSACTIONS of the ASAE*, vol. 6, no. 1, pp. 108-114.
- Cunningham, F.M. & Chao, E.Y.S. 1967, "Design relationships for centrifugal fertilizer distributors", *TRANSACTIONS of the ASAE*, vol. 10, no. 1, pp. 91-95.
- Dintwa, E., Tijskens, E., Olieslagers, R., Baerdemaeker, J.D. & Ramon, H. 2004, "Calibration of a Spinning Disc Spreader Simulation Model for Accurate Site-specific Fertiliser Application", *Biosystems Engineering*, vol. 88, no. 1, pp. 49-62.
- Dintwa, E., Van Liedekerke, P., Olieslagers, R., Tijskens, E. & Ramon, H. 2004, "Model for Simulation of Particle Flow on a Centrifugal Fertiliser Spreader", *Biosystems Engineering*, vol. 87, no. 4, pp. 407-415.
- Fulton, J.P., Shearer, S.A., Chabra, G. & Higgins, S.F. 2001, "Performance assessment and model development of a variable-rate, spinner-disc fertilizer applicator", *Transactions of the American Society of Agricultural Engineers*, vol. 44, no. 5, pp. 1071-1081.
- Griffis, C.L., Ritter, D.W. & Matthews, E.J. 1983, "SIMULATION OF ROTARY SPREADER DISTRIBUTION PATTERNS", *Transactions of the American Society of Agricultural Engineers*, vol. 26, no. 1, pp. 33-37.

- Grift, T.E. & Hofstee, J.W. 1997, "Measurement of Velocity and Diameter of Individual Fertilizer Particles by an Optical Method", *Journal of Agricultural Engineering Research*, vol. 66, no. 3, pp. 235-238.
- Grift, T.E. & Kweon, G. 2006, "Development of a Uniformity Controlled Granular Fertilizer Spreader", *ASAE Paper No. 061069. St. Joseph, Mich.*
- Hofstee, J.W. 1995, "Handling and Spreading of Fertilizers: Part 5, The Spinning Disc Type Fertilizer Spreader", *Journal of Agricultural Engineering Research*, vol. 62, no. 3, pp. 143-162.
- Hofstee, J.W. 1994, "Handling and Spreading of Fertilizers: Part 3, Measurement of Particle Velocities and Directions with Ultrasonic Transducers, Theory, Measurement System, and Experimental Arrangements", *Journal of Agricultural Engineering Research*, vol. 58, no. 1, pp. 1-16.
- Hofstee, J.W. & Huisman, W. 1990, "Handling and spreading of fertilizers part 1: Physical properties of fertilizer in relation to particle motion", *Journal of Agricultural Engineering Research*, vol. 47, no. 0, pp. 213-234.
- Inns, F.M. & Reece, A.R. 1962, "The theory of the centrifugal distributor II: motion on the disc, off-centre feed", *Journal of Agricultural Engineering Research*, vol. 4, no. 7, pp. 345-353.
- Kuo, H.P., Knight, P.C., Parker, D.J., Adams, M.J. & Seville, J.P.K. 2004, "Discrete element simulations of a high-shear mixer", *Advanced Powder Technology*, vol. 15, no. 3, pp. 297-309.
- Lv, H., Yu, J. & Fu, H. 2013, "Simulation of the operation of a fertilizer spreader based on an outer groove wheel using a discrete element method", *Mathematical and Computer Modelling*, vol. 58, no. 3-4, pp. 842-851.
- Mennel, R.M. & Reece, A.R. 1963, "The theory of the centrifugal distributor. III: Particle trajectories", *Journal of Agricultural Engineering Research*, vol. 7, no. 3, pp. 78-84.
- Olieslagers, R. 1997, "Fertilizer distribution modelling for centrifugal spreader design", *PhD Thesis, Faculteit Landbouwkundige en Toegepaste Biologische Wetenschappen, K. U. Leuven, Belgium.*
- Olieslagers, R., Ramon, H. & De Baerdemaeker, J. 1996, "Calculation of Fertilizer Distribution Patterns from a Spinning Disc Spreader by means of a Simulation Model", *Journal of Agricultural Engineering Research*, vol. 63, no. 2, pp. 137-152.
- Patterson, D.E. & Reece, A.R. 1962, "The theory of the centrifugal distributor. I: Motion on the disc, near-centre feed", *Journal of Agricultural Engineering Research*, vol. 7, no. 3, pp. 232-240.
- Pitt, R.E., Farmer, G.S. & Walker, L.P. 1982, "APPROXIMATING EQUATIONS FOR ROTARY DISTRIBUTOR SPREAD PATTERNS", *Transactions of the American Society of Agricultural Engineers*, vol. 25, no. 6, pp. 1544-1552.
- RAUCH 2014. *Products*. [Online] Available at: http://alt.rauch.de/front_content.php [Accessed 05 May 2014].
- Reints, R. E. & Yoerger, R. R. 1967, "Trajectories of seeds and granular fertilizers" *Transactions of the ASAE*, vol. 10, no. 2, pp. 213-216.

- Reumers, J., Tijskens, E. & Ramon, H. 2003, "Experimental Characterisation of the Tangential and Cylindrical Fertiliser Distribution Pattern from a Spinning Disc: A Parameter Study", *Biosystems Engineering*, vol. 86, no. 3, pp. 327-337.
- Salt Association 2014. *De-icing - Keeping our roads open*. [Online] Available at: <http://saltassociation.co.uk/de-icing-roads/> [Accessed 10 June 2014].
- Stewart, R.L., Bridgwater, J., Zhou, Y.C. & Yu, A.B. 2001, "Simulated and measured flow of granules in a bladed mixer—a detailed comparison", *Chemical Engineering Science*, vol. 56, no. 19, pp. 5457-5471.
- Strøm, J.S. 2012, "Standardization of test method for salt spreader: Air flow experiments. Report 9: Visualization of airflow patterns behind a full scale salt truck ", *Aarhus University, Engineering Centre Bygholm, Test and Development*.
- Strøm, J.S. 2012, "Standardisation of test method for salt spreader: Air flow experiments. Report 7: Effect of crosswind on salt distribution", *Aarhus University, Engineering Centre Bygholm, Test and Development*.
- Strøm, J.S. 2012, "Standardization of test method for salt spreader: Air flow experiments. Report 11: Methods to reduce large eddy turbulence behind a salt truck", *Aarhus University, Engineering Centre Bygholm, Test and Development*.
- Takai, H. 2013, "Standardization of test method for salt spreader: Air flow experiment. Report 8: Observations of salt particle trajectory from spreader disc to road surface", *Aarhus University, Engineering Centre Bygholm, Test and Development*.
- Takai, H. 2013, "Standardization of test method for salt spreader: Air flow experiment. Report 10: Simulation of salt particle trajectory from spreader disc to road surface. Basic consideration and equations", *Aarhus University, Engineering Centre Bygholm, Test and Development*.
- Tijskens, E., Loodts, J., Van Zeebroeck, M., Van Liedekerke, P., Dintwa, E. & Ramon, H. 2004, "Particle Based Simulations with DEMeter++", *Proceedings of Partec2004, International Conference for Particle Technology, 16-18 March*.
- UNIA in Romania 2013. *Utility machines*. [Online] Available at: <http://www.unia.ro/en> [Accessed 05 May 2014].
- Van Liedekerke, P., Piron, E., Vangeyte, J., Villette, S., Ramon, H. & Tijskens, E. 2008, "Recent results of experimentation and DEM modeling of centrifugal fertilizer spreading", *Granular Matter*, vol. 10, no. 4, pp. 247-255.
- Van Liedekerke, P., Tijskens, E., Dintwa, E., Anthonis, J. & Ramon, H. 2006, "A discrete element model for simulation of a spinning disc fertilizer spreader I. Single particle simulations", *Powder Technology*, vol. 170, no. 2, pp. 71-85.
- Van Liedekerke, P., Tijskens, E., Dintwa, E., Rioual, F., Vangeyte, J. & Ramon, H. 2009, "DEM simulations of the particle flow on a centrifugal fertilizer spreader", *Powder Technology*, vol. 190, no. 3, pp. 348-360.
- Van Liedekerke, P., Tijskens, E. & Ramon, H. 2009, "Discrete element simulations of the influence of fertiliser physical properties on the spread pattern from spinning disc spreaders", *Biosystems Engineering*, vol. 102, no. 4, pp. 392-405.
- J. Vangeyte, B. Sonck, P. Van Liedekerke, H. Ramon, "Comparison of two methods to measure the outlet velocity of fertiliser grains from a rotary disc", *Proceedings of AgEng 2004*. 12-16 September 2004, Leuven, Belgium. 336-337.

- Villar, G.C., Menezes, J.C. & Donadon, M.V. 2012, "Accuracy and numerical stability of direct time integration schemes applied to rotordynamics", 12th Pan-American Congress of Applied Mechanics, Port of Spain, Trinidad, 02/06.
- Villasuso, J. 2003. *Recursos de física*. [Online] Available at: <http://teleformacion.edu.aytolacoruna.es/FISICA/document/index.htm> [Accessed 17 July 2014].
- Villette, S., Cointault, F., Piron, E. & Chopinet, B. 2005, "Centrifugal Spreading: an Analytical Model for the Motion of Fertiliser Particles on a Spinning Disc", *Biosystems Engineering*, vol. 92, no. 2, pp. 157-164.
- Villette, S., Piron, E., Cointault, F. & Chopinet, B. 2008, "Centrifugal spreading of fertiliser: Deducing three-dimensional velocities from horizontal outlet angles using computer vision", *Biosystems Engineering*, vol. 99, no. 4, pp. 496-507.
- Villette, S., Piron, E., Miclet, D., Martin, R., Jones, G., Paoli, J. & Gée, C. 2012, "How mass flow and rotational speed affect fertiliser centrifugal spreading: Potential interpretation in terms of the amount of fertiliser per vane", *Biosystems Engineering*, vol. 111, no. 1, pp. 133-138.
- Weast, R.C. & Astle, M.J. 1981-1982, *CRC Handbook of Chemistry and Physics*, 62nd edn, CRC Press, Boca raton, Florida.
- Xie, Y.M. 1996, "AN ASSESSMENT OF TIME INTEGRATION SCHEMES FOR NON-LINEAR DYNAMIC EQUATIONS", *Journal of Sound and Vibration*, vol. 192, no. 1, pp. 321-331.
- Yule I.J. 2011. "The Effect of Fertiliser Particle Size on Spread Distribution", *NZ Centre for Precision Agriculture, Massey University, Palmerston North, New Zealand*, no.24 .
- Zhou, Y.C., Yu, A.B., Stewart, R.L. & Bridgwater, J. 2004, "Microdynamic analysis of the particle flow in a cylindrical bladed mixer", *Chemical Engineering Science*, vol. 59, no. 6, pp. 1343-1364.

5.2. Software

- MATLAB® Registered trademark of The MathWorks Inc., Natick, MA, USA www.mathworks.se
- AutoCAD® Registered trademark of Autodesk Inc., San Rafael, CA, USA www.autodesk.com

6. Annexes

6.1. Frame processing

For the five rotation speed studied, this annex outlines the following frame processing elements:

- Frame selection.
- Graphical location of the points of interest along the vane and their projections over the horizontal plane of reference.
- Coordinates of these points of interest.
- Definition of the line segments which join the points of interest.
- Proportion of the total flow to be collected by the vane in the corresponding frame.
- Graphical identification of sections with different salt density and definition of their respective coefficients of compaction C_c .
- Coordinates of the borderlines separating the identified density sections.

6.1.1. Rotation speed of the disk: 80 rpm

Analogous points from the high speed video frame over the horizontal plane of reference

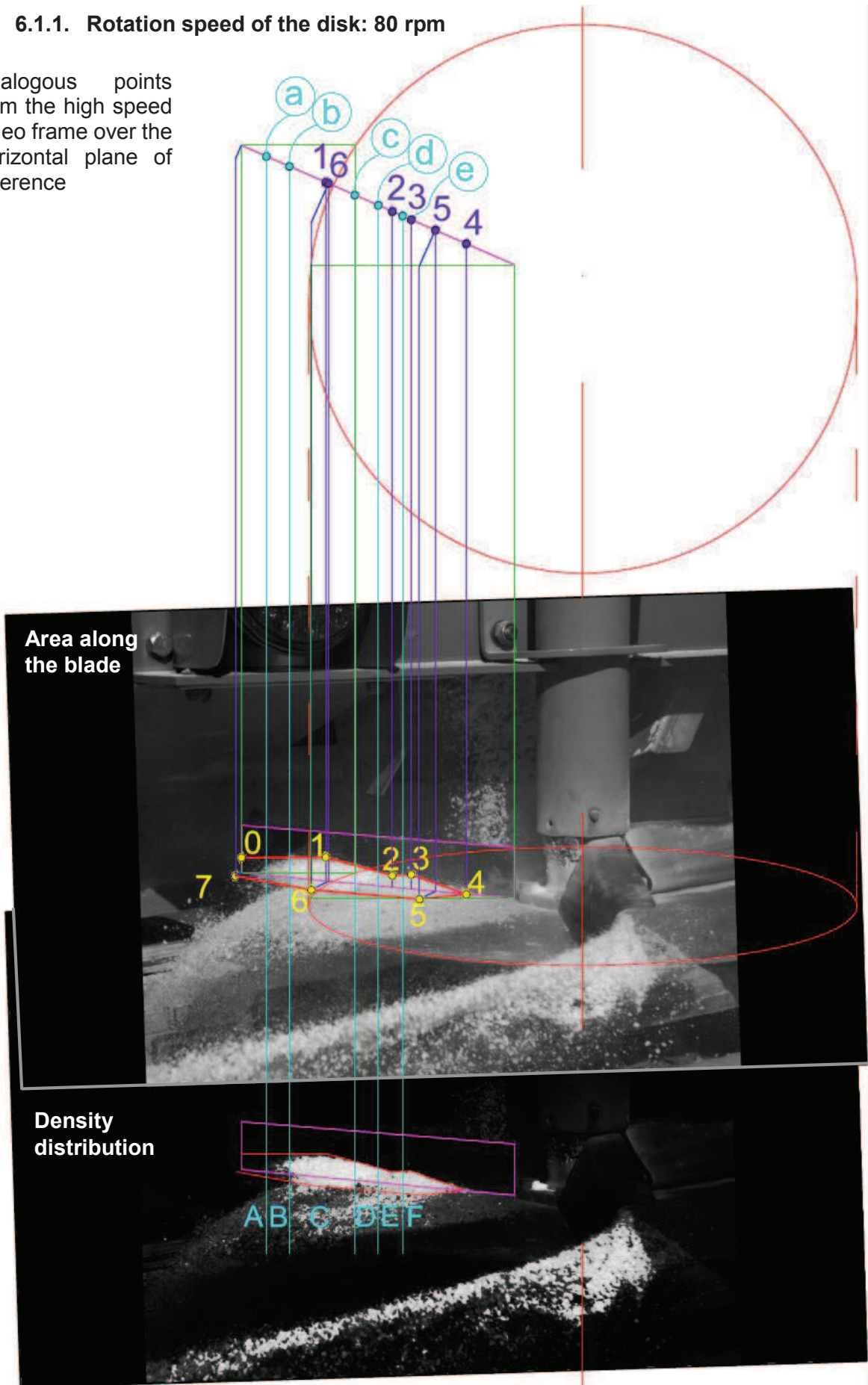


Figure 40. Image processing - 80rpm

- Points of interest in cylindrical coordinates

In the $\rho\varphi$ -plane:

Table 9. Cylindrical coordinates of the points of interest - 80rpm

	5	6	7
ρ (m)	0,08171	0,1915	0,2810
φ (m)	0,0369	0,0405	0,01429

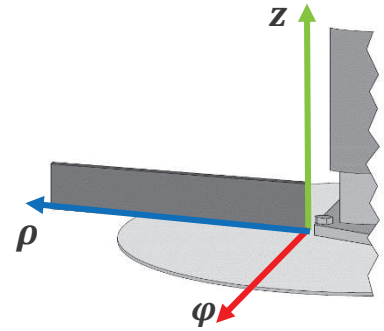


Figure 41. Axis legend

In the ρz -plane:

	0	1	2	3	4
ρ (m)	0,2810	0,1944	0,1258	0,1064	0,0499
z (m)	0,0161	0,0243	0,0119	0,0145	0,00

- Line segments

Table 11. Line segments parameters m and c - 80rpm

Line	Function	m	c
0-1	$z = m\rho + c$	-0,0944	0,0427
1-2		0,1813	-0,0109
2-3		-0,1330	0,0286
3-4		0,2562	-0,0128
4-5	$\varphi = m\rho + c$	1,1621	-0,0580
5-6		0,0327	0,0343
6-7		-0,2931	0,0966

- Effective Flow

Assumption of percentage collected by the vane in the selected frame:

Table 10. Mass flow estimate - 80rpm

%	Mass flow (kg/s)
45	438,34

- Density estimates

Table 12. Coefficient of compaction distribution - 80rpm

Section	Density solid salt (kg/m ³)	C_c	Density sub-domain (kg/m ³)
A	2165	0,20	433
B		0,40	866
C		0,90	1948,5
D		0,85	1840,25
E		0,65	1407,25
F		0,75	1623,75

Location of the borderlines along the vane:

Table 13. Division of density sections - 80rpm

	a	b	c	d	e
ρ (m)	0,2554	0,2317	0,1644	0,1403	0,1154

6.1.2. Rotation speed of the disk: 100 rpm

Analogous points from the high speed video frame over the horizontal plane of reference

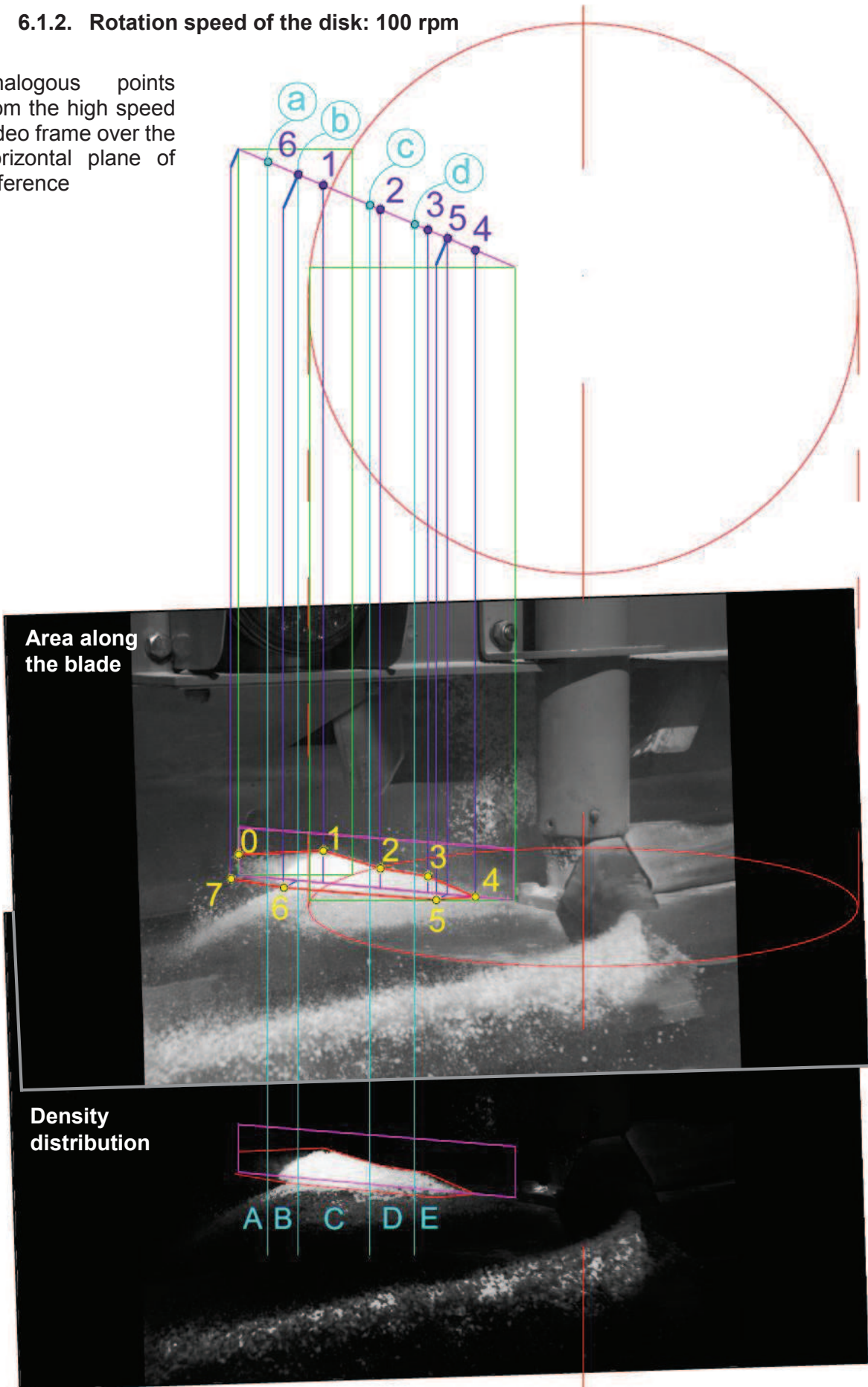


Figure 42. Image processing - 100rpm

- Points of interest in cylindrical coordinates

In the $\rho\varphi$ -plane:

Table 14. Cylindrical coordinates of the points of interest - 100rpm

	5	6	7
ρ (m)	0,0684	0,2205	0,2810
φ (m)	0,027	0,0341	0,0180

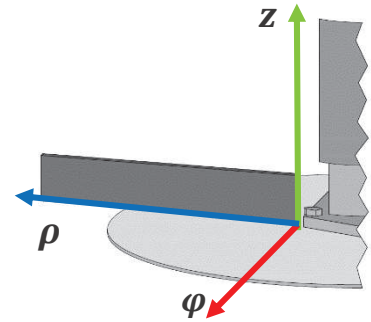


Figure 43. Axis legend

In the ρz -plane:

	0	1	2	3	4
ρ (m)	0,2810	0,1950	0,1369	0,0885	0,0401
z (m)	0,0215	0,0329	0,0198	0,0162	0,00

- Line segments

Table 16. Line segments parameters m and c - 100rpm

Line	Function	m	c
0-1	$z = m\rho + c$	-0,1323	0,0568
1-2		0,2254	-1,1085
2-3		0,0729	0,9799
3-4		0,3356	-1,3455
4-5	$\varphi = m\rho + c$	0,9537	-0,0382
5-6		0,0467	0,0238
6-7		-0,2664	0,0928

- Effective Flow

Assumption of percentage collected by the vane in the selected frame:

Table 15. Mass flow estimate - 100rpm

%	Mass flow (kg/s)
60	584,45

- Density estimates

Table 17. Coefficient of compaction distribution - 100rpm

Section	Density solid salt (kg/m ³)	C_c	Density sub-domain (kg/m ³)
A	2165	0,15	324,75
B		0,50	1082,5
C		0,90	1948,5
D		0,80	1732
E		0,70	1515,5

Location of the borderlines along the vane:

Table 18. Division of density sections - 100rpm

	a	b	c	d
ρ (m)	0,2511	0,2204	0,1475	0,1018

6.1.3. Rotation speed of the disk: 160 rpm

Analogous points from the high speed video frame over the horizontal plane of reference

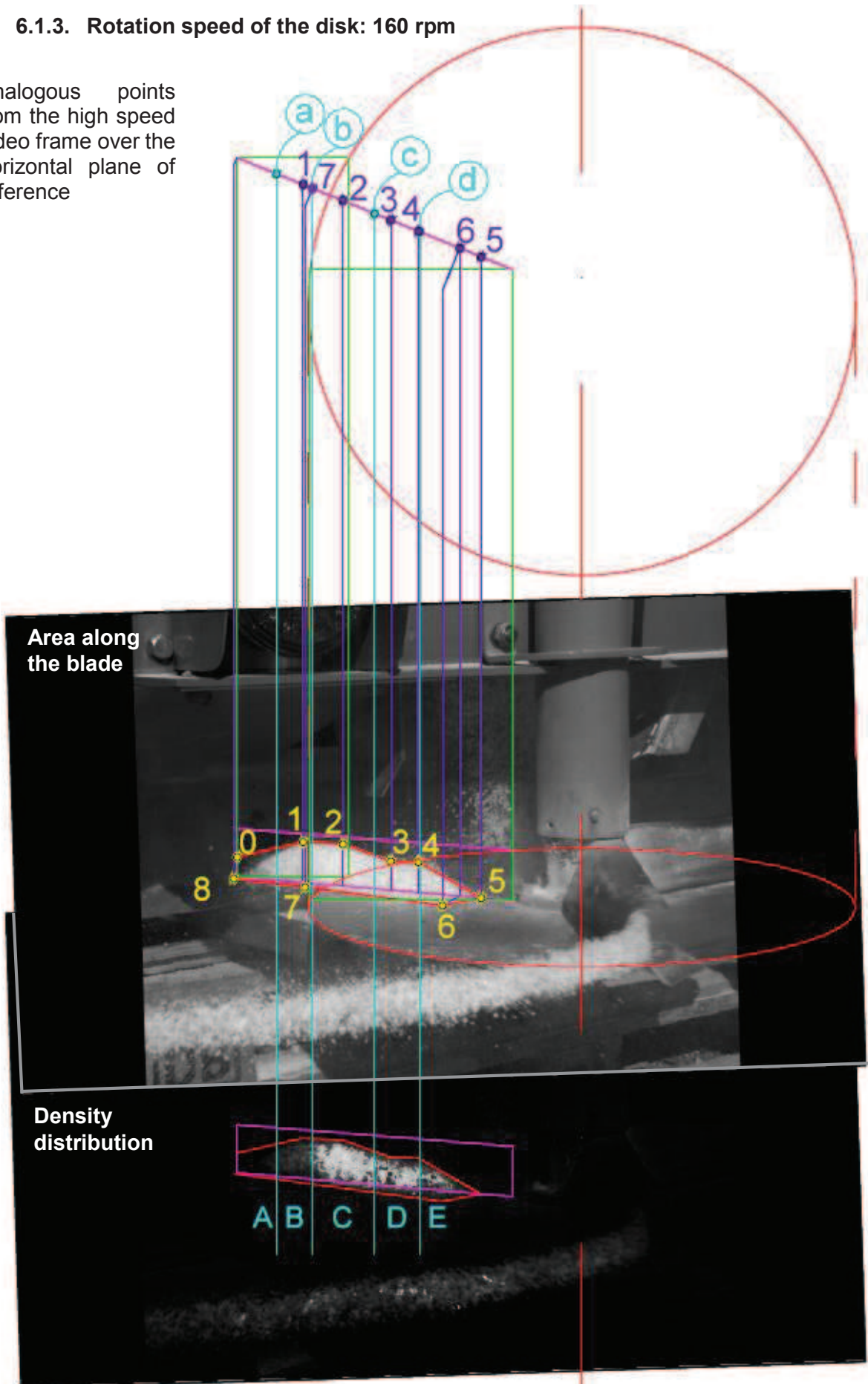


Figure 44. Image processing - 160rpm

- Points of interest in cylindrical coordinates

In the $\rho\varphi$ -plane:

Table 19. Cylindrical coordinates of the points of interest - 160rpm

	6	7	8
ρ (m)	0,0539	0,2040	0,281
φ (m)	0,0435	0,0186	0,0080

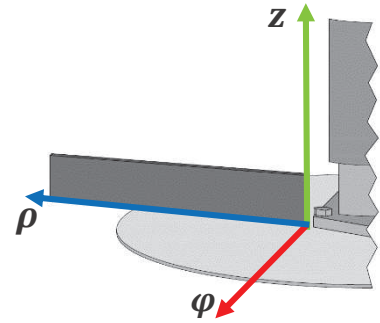


Figure 45. Axis legend

In the ρz -plane:

	0	1	2	3	4	5
ρ (m)	0,2810	0,2136	0,1734	0,1243	0,0961	0,0322
z (m)	0,0204	0,0417	0,0429	0,0292	0,0307	0,00

- Line segments

Table 21. Line segments parameters m and c – 160rpm

Line	Function	m	c
0-1	$z = m\rho + c$	-0,3154	0,1091
1-2		-0,0293	0,0480
2-3		0,2780	-0,0053
3-4		-0,0506	0,0355
4-5		0,4796	-0,0154
5-6	$\varphi = m\rho + c$	2,0060	-0,0646
6-7		-0,1664	0,0525
7-8		-0,1366	0,0464

- Effective Flow

Assumption of percentage collected by the vane in the selected frame:

Table 20. Mass flow estimate - 160rpm

%	Mass flow (kg/s)
87	847,45

- Density estimates

Table 22. Coefficient of compaction distribution – 160rpm

Section	Density solid salt (kg/m ³)	C_c	Density sub-domain (kg/m ³)
A	2165	0,30	649,5
B		0,40	866
C		0,90	1948,5
D		0,80	1732
E		0,70	1515,5

Location of the borderlines along the vane:

Table 23. Division of density sections – 160rpm

	a	b	c	d
ρ (m)	0,2408	0,2040	0,1411	0,0949

6.1.4. Rotation speed of the disk: 190 rpm

Analogous points from the high speed video frame over the horizontal plane of reference

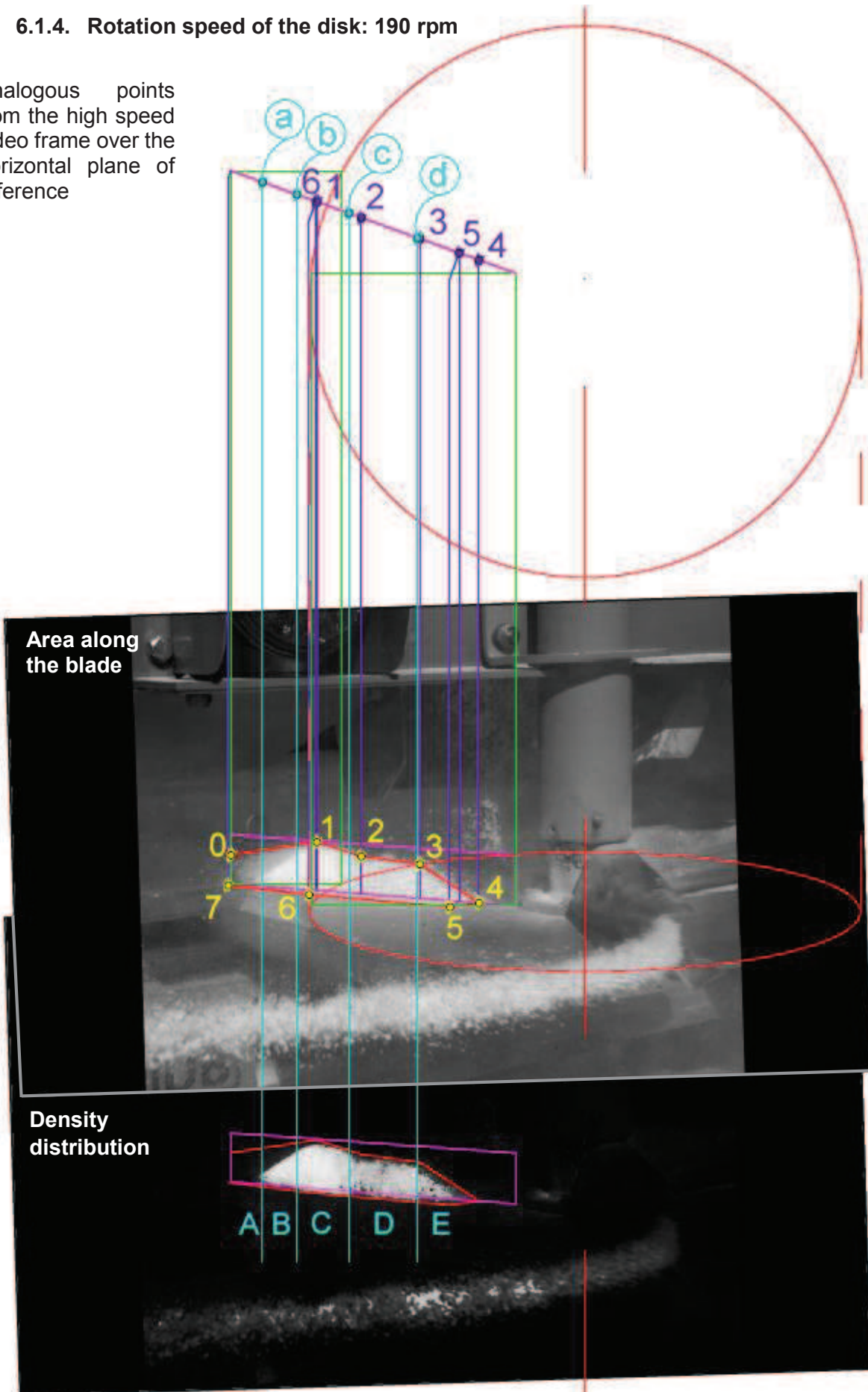


Figure 46. Image processing - 190rpm

- Points of interest in cylindrical coordinates

In the $\rho\varphi$ -plane:

Table 24. Cylindrical coordinates of the points of interest - 190rpm

	5	6	7
ρ (m)	0,0561	0,1970	0,281
φ (m)	0,0254	0,0190	0,007

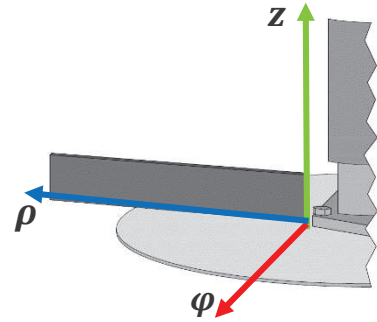


Figure 47. Axis legend

In the ρz -plane:

	0	1	2	3	4
ρ (m)	0,2810	0,1960	0,1524	0,0948	0,0365
Y (m)	0,0295	0,0490	0,0377	0,0342	0,00

- Line segments

Table 26. Line segments parameters m and c - 190rpm

Line	Function	m	c
0-1	$z = m\rho + c$	-0,2300	0,0941
1-2		0,2590	-0,0018
2-3		0,0604	0,0285
3-4		0,5878	-0,0215
4-5	$\varphi = m\rho + c$	1,2996	-0,0475
5-6		-0,0454	0,0279
6-7		-0,1441	0,0474

- Effective Flow

Assumption of percentage collected by the vane in the selected frame:

Table 25. Mass flow estimate - 190rpm

%	Mass flow (kg/s)
93	905,89

- Density estimates

Table 27. Coefficient of compaction distribution - 190rpm

Section	Density solid salt (kg/m ³)	C_c	Density sub-domain (kg/m ³)
A	2165	0,25	541,25
B		0,65	1407,25
C		0,90	1948,5
D		0,70	1515,5
E		0,60	1299

Location of the borderlines along the vane:

Table 28. Division of density sections - 190rpm

	a	b	c	d
ρ (m)	0,2497	0,2159	0,1647	0,0972

6.1.5. Rotation speed of the disk: 215 rpm

Analogous points from the high speed video frame over the horizontal plane of reference

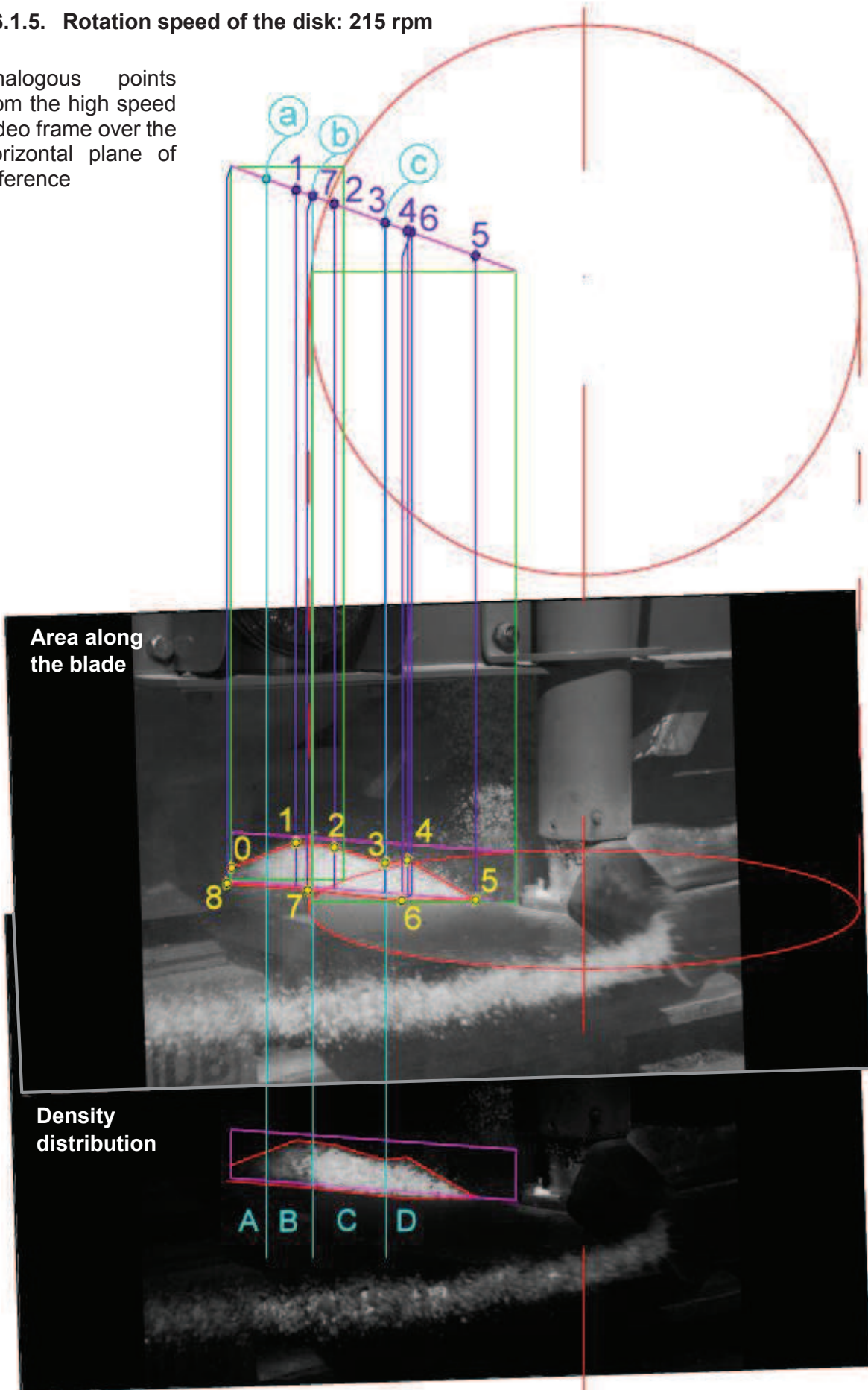


Figure 48. Image processing - 215rpm

- Points of interest in cylindrical coordinates

In the $\rho\varphi$ -plane:

Table 29. Cylindrical coordinates of the points of interest - 215rpm

	6	7	8
ρ (m)	0,1033	0,2008	0,281
φ (m)	0,0253	0,0139	0,0121

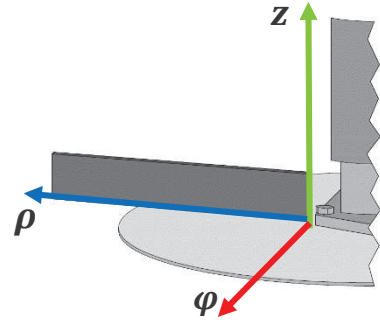


Figure 49. Axis legend

In the ρz -plane:

	0	1	2	3	4	5
ρ (m)	0,2810	0,2174	0,1797	0,1294	0,1073	0,0401
z (m)	0,0134	0,0437	0,0420	0,0298	0,0344	0,00

- Line segments

Table 31. Line segments parameters m and c - 215rpm

Line	Function	m	c
0-1	$z = m\rho + c$	-0,4766	0,1474
1-2		0,0458	0,0338
2-3		0,2431	-0,0017
3-4		-0,2058	0,0564
4-5		0,5110	-0,0205
5-6	$\varphi = m\rho + c$	0,4003	-0,0160
6-7		-0,1173	0,0375
7-8		-0,0227	0,0184

- Effective Flow

Assumption of percentage collected by the vane in the selected frame:

Table 30. Mass flow estimate - 215rpm

%	Mass flow (kg/s)
95	925,38

- Density estimates

Table 32. Coefficient of compaction distribution - 215rpm

Section	Density solid salt (kg/m ³)	C_c	Density sub-domain (kg/m ³)
A	2165	0,30	649,5
B		0,70	1515,5
C		0,90	1948,5
D		0,80	1732

Location of the borderlines along the vane:

Table 33. Division of density sections - 215rpm

	a	b	c
ρ (m)	0,2468	0,2008	0,1282

6.2. Extracted data for the radial velocity and model fitting

This annex contains the extracted data for the radial velocity that are obtained from processing of frames from high speed videos along with the model fitting. Extracted data points and the fitted model are presented in a series of graphs where the ordinate represents the radial velocity, $\dot{\rho}$, and the abscissa the position of the sub-domain, ρ , along the vane.

6.2.1. Rotation speed of the disk: 80 rpm

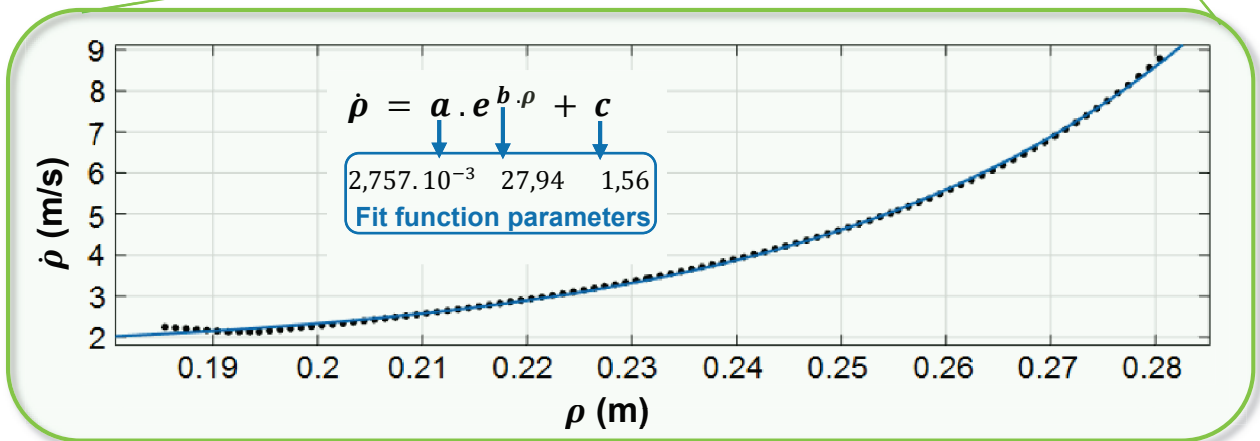
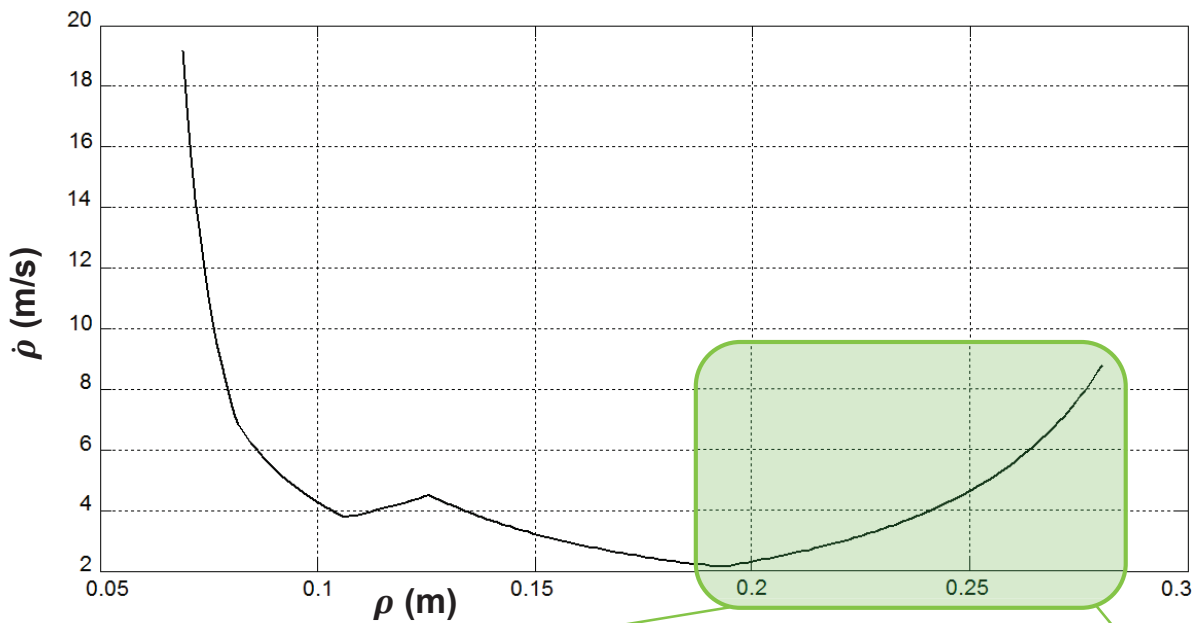


Figure 50. Radial velocity data and model fitting - 80rpm

6.2.2. Rotation speed of the disk: 100 rpm

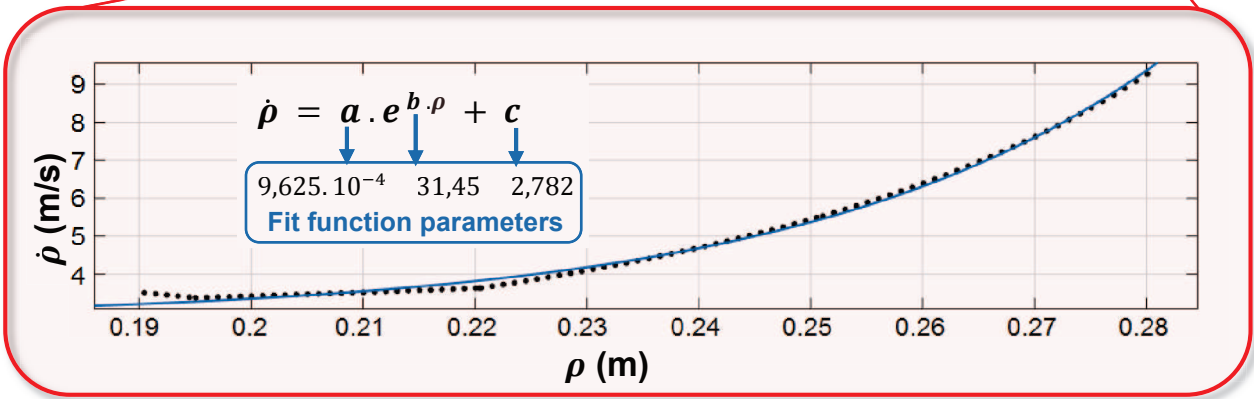
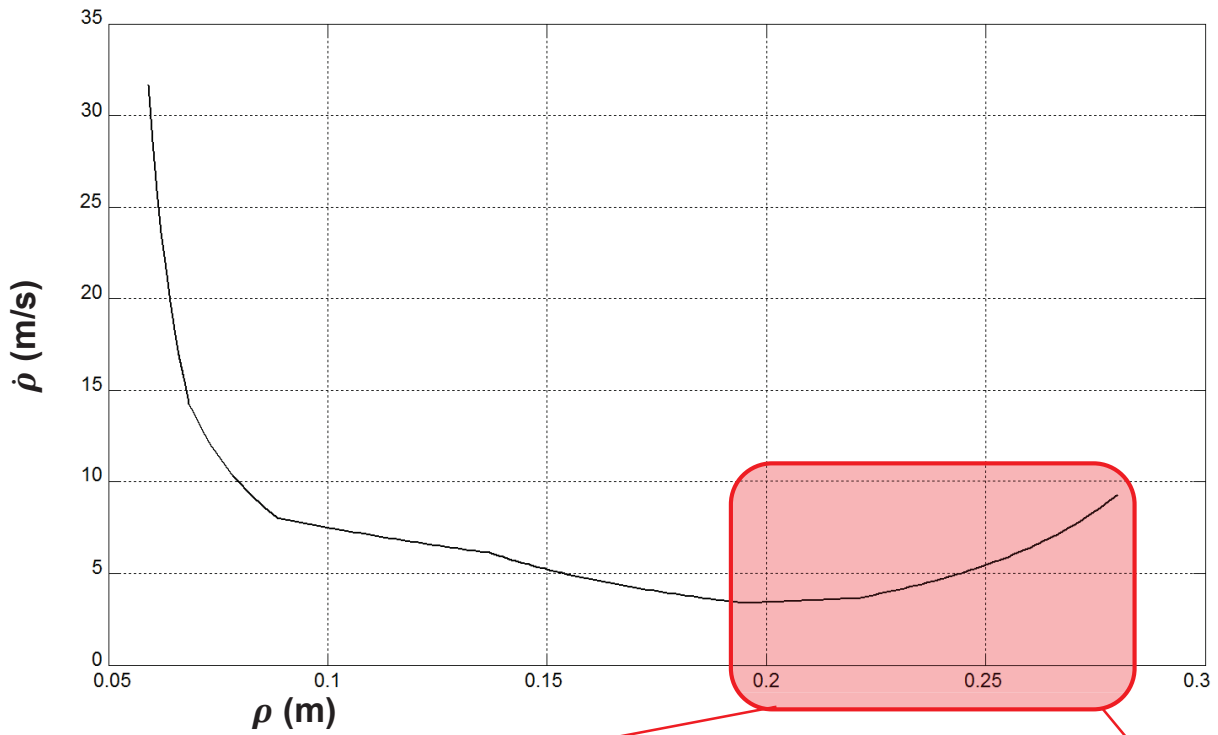


Figure 51. Radial velocity data and model fitting - 100rpm

6.2.3. Rotation speed of the disk: 160 rpm

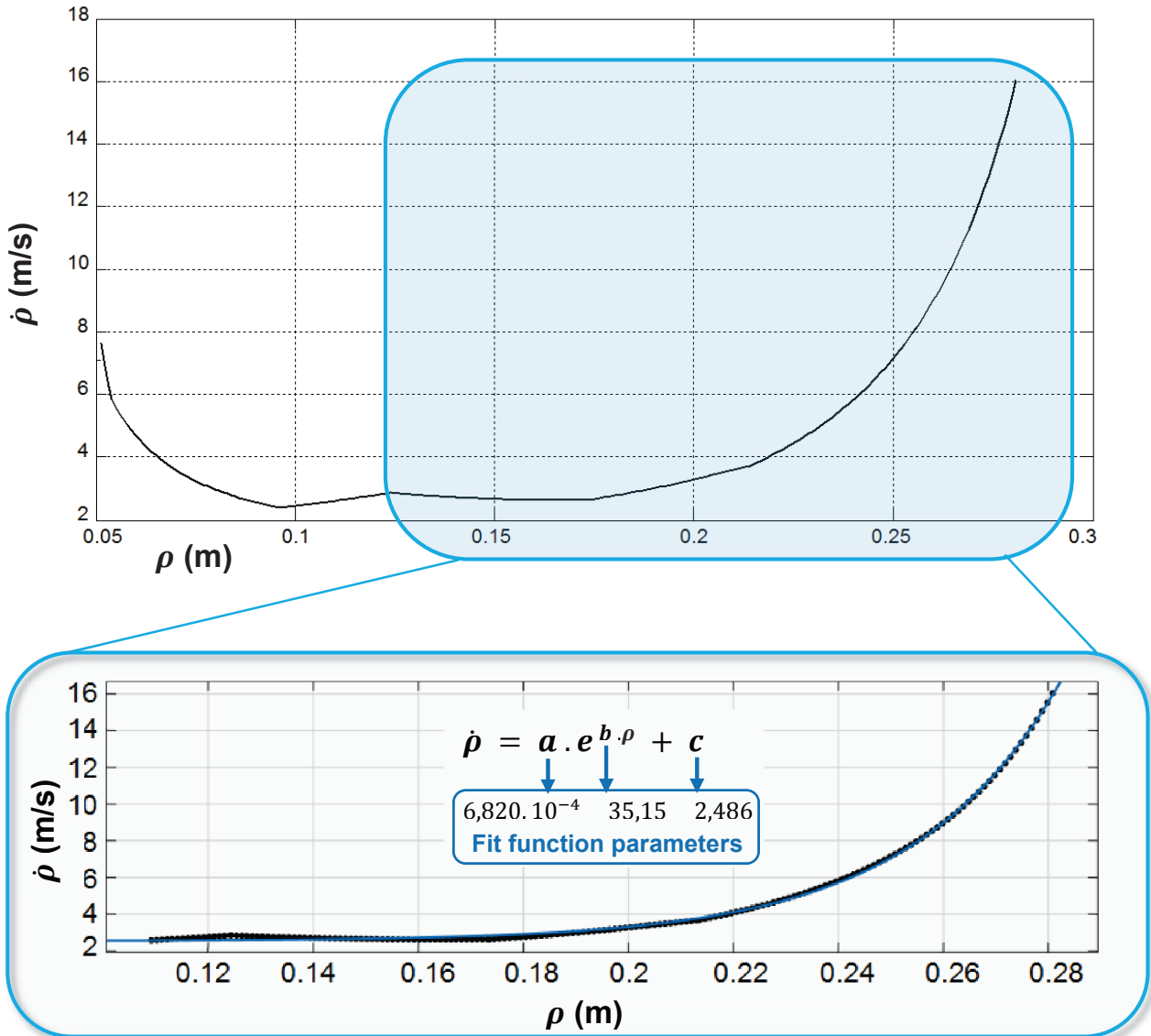


Figure 52. Radial velocity data and model fitting - 160rpm

6.2.4. Rotation speed of the disk: 190 rpm

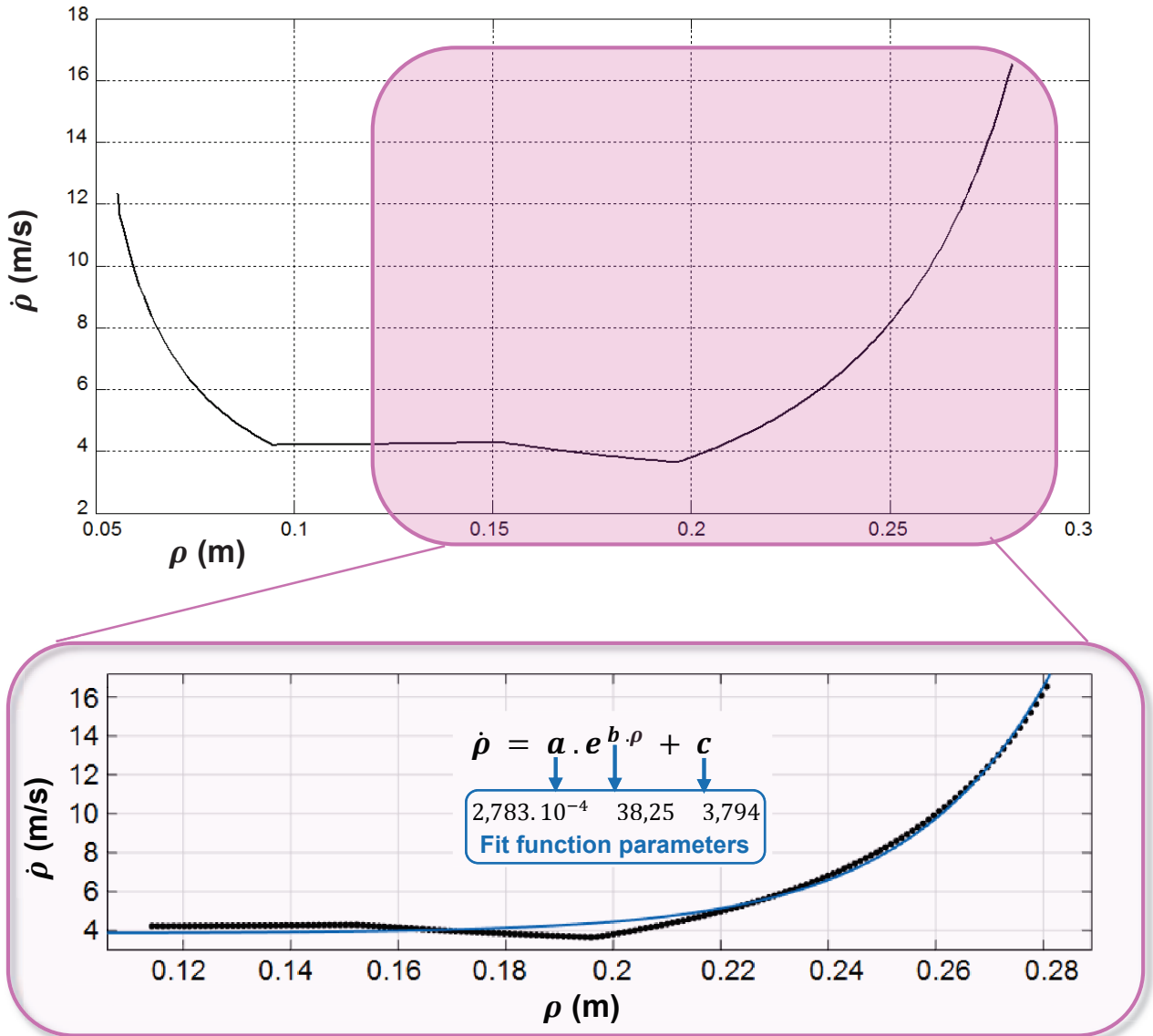


Figure 53. Radial velocity data and model fitting - 190rpm

6.2.5. Rotation speed of the disk: 215 rpm

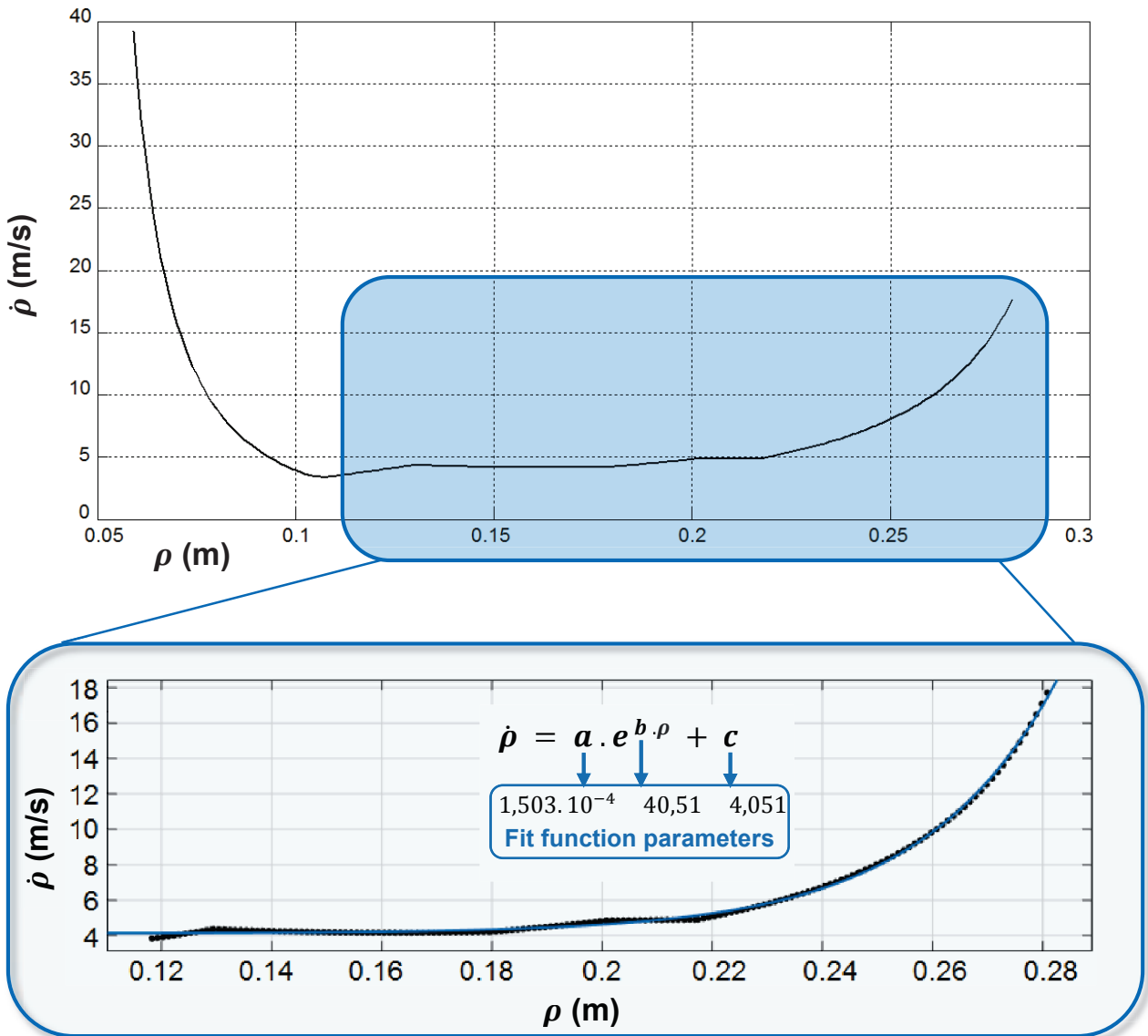


Figure 54. Radial velocity data and model fitting - 215rpm

6.3. MATLAB® codes

6.3.1. Analytic solution vs Newmark average acceleration solution

Comparison between analytical and Newmark solution (see section 1.2)

- **Comparison**

```
function [U,depl,vel,accl,t]=Comparison(M,C,K,P,Xo,Xpo,type)
%%IMPUTS
%   M - Mass matrix
%   K - Stiffness matrix
%   C - Damping matrix
%   P - Force matrix
%   type - Type of Newmark's method to be used (average vs linear)
%%IN USE
%   zi - Damping factor
%   w - Natural frequency of the system
%   Xo - displacement t=0
%   Xpo - velocity t=0
%   depl - system displacement
%   vel - system velocities
%   accl - system accelerations

ti = 0. ;
tf = 1. ;
dt = 0.001 ;
t = ti:dt:tf ;
nt = fix((tf-ti)/dt) ;

%% Analytic solution
w=sqrt(K/M);
zi=C/(2*M*w);
if zi<1
    wd=w*sqrt(1-zi*zi);A=Xo;B=(Xpo+zi*w*A)/wd;
    q1=(A*cos(wd*t)+B*sin(wd*t));q2=exp(-zi*w*t);
    U=q2.*q1;
elseif zi==1
    A=Xo;B=Xpo+A*w;
    U=(B*t+A).*exp(-w*t);
else
    landa1=-zi*w+w*sqrt(zi*zi-1);landa2=-zi*w-w*sqrt(zi*zi-1);
    A=((Xo*landa2)-Xpo)/(landa2-landa1);
    B=(Xpo-(Xo*landa1))/(landa2-landa1);
    U=A*exp(landa1*t)+B*exp(landa2*t);
end
end
plot (t,U,'g')
xlabel ('t'); ylabel ('x')
hold on

%% Newmark's method
switch type
case 'Average'
    gaama = 1/2 ;beta = 1/4 ;
case 'Linear'
    gaama = 1/2 ;beta = 1/6 ;
end
```

```

% Constants used
a1 = gaama/(beta*dt) ; a2 = 1/(beta*dt^2) ;
a3 = 1/(beta*dt) ;    a4 = gaama/beta ;
a5 = 1/(2*beta) ;    a6 = ((gaama/(2*beta))-1)*dt ;

%Dimensions
depl = zeros(1,nt) ;
vel = zeros(1,nt) ;
accl = zeros(1,nt) ;

% Initial conditions
depl(:,1) = Xo ;
vel(:,1) = Xpo ;
P0 = zeros(1,1) ;
accl(:,1) = (P-C*vel(:,1)-K*depl(:,1))/M ;
a = a3*M+a4*C ;
b = a5*M+a6*C ;

% Effective stiffness matrix
Kcap = K+a1*C+a2*M ;

% Time step starts
for i = 1:nt
    delP = P0+a*vel(:,i)+b*accl(:,i) ;
    delu = delP/Kcap ;
    delv = a1*delu-a4*vel(:,i)-a6*accl(:,i) ;
    dela = a2*delu-a3*vel(:,i)-a5*accl(:,i) ;
    depl(:,i+1) = depl(:,i)+delu ;
    vel(:,i+1) = vel(:,i)+delv ;
    accl(:,i+1) = accl(:,i)+dela ;
end

plot (t,depl,'r')
grid on

%%Error
ERRORy=abs(abs(depl)-abs(U));
MAXERRORy=(max(max(abs(ERRORy))))

end

```

6.3.2. Newmark average acceleration algorithm

- **NewmarkSecondOrderPerturbation**

%Torben Brøchner, 2014

```

function ...
[ qROC0, qROC1, qROC2 ] ...
= ii_NewmarkSecondOrderPerturbation...
( qROC0, qROC1, qROC2, qROC2_Delta, h )

qROC0 = qROC0 + qROC1*h + qROC2*h*h/2 + qROC2_Delta*h*h/4;
qROC1 = qROC1 + qROC2*h + qROC2_Delta*h/2;
qROC2 = qROC2 + qROC2_Delta;
end

```

6.3.3. Newmark approach incorporating radial scaling function

- **Rusty Robert**

%Torben Brøchner & Paula Macías, 2014

%% Arrays

N=1000;

% time array

t=zeros(N,1);

% 2D r-phi arrays

r=zeros(N,4);

phi=zeros(N,1);

vr=zeros(N,1);

vphi=zeros(N,1);

ar=zeros(N,1);

aphi=zeros(N,1);

% 2D x-y arrays

rx=zeros(N,2);

vxy=zeros(N,2);

axy=zeros(N,2);

% Results array for pos, vel & acc in x-y

Xxy=zeros(N,9);

%% Constants

StartAngle=0.0;

wn=80;

w=wn*2*pi/60;

TauProportion=0.5; ;

Tau=2*pi/w*TauProportion;

Dt=Tau/N;

Dphi=w*Dt;

tanDphi=tan(Dphi);

% Start angle [rad]

% [rev/min]

% Angular speed [rad/s]

% Time before leaving the disk (relative)

% Period on disk [s]

% Time increment "Tau" [s]

% Angle Increment "delta-phi" [rad]

% "Tangent delta-phi" [-]

%% Initial values

t(1)=0;

r(1,1)=0.14; % r

r(1,2)=0.0; % r'

r(1,3)=0; % r''

r(1,4)=0; % Dr''

% Position

phi(1,1)=2*pi*StartAngle;

% Velocity

vr(1,1)=0;

vphi(1,1)=0;

% Acceleration

ar(1,1)=0;

aphi(1,1)=0;

%% Loop

for i=1:N

```

%% - Time an angle incrementation
t(i+1)=t(i)+Dt;
phi(i+1)=phi(i)+Dphi;

%% - Basic estimates in r-phi
r(i+1,2)=r(i,1)*w*tanDphi*RadialScalingFunction(i); % r' estimate
r(i+1,3)=(r(i+1,2)-r(i,2))/Dt; % r'' estimate
r(i+1,4)=r(i+1,3)-r(i,3); % Dr'' estimate

%% - Newmark extrapolations - radial dir. only
[r(i+1,1),r(i+1,2),r(i+1,3)]=...
    ii_NewmarkSecondOrderPerturbation...
    ( r(i,1), r(i,2), r(i,3), r(i+1,4), Dt);

%% - Velocity in r-phi
vr(i+1,1)=r(i+1,2);
vphi(i+1,1)=r(i+1,1)*w;

%% - Acceleration in r-phi
ar(i+1,1)=r(i+1,3)-r(i+1,1)*w*w;
aphi(i+1,1)=2*r(i+1,2)*w;

%% - COORDINATE TRANSFORMATION from r-phi to x-y
%% - Position in x-y

Xxy(i+1,1)=r(i+1,1)*cos(phi(i+1));
Xxy(i+1,2)=r(i+1,1)*sin(phi(i+1));

% Rotation matrix r-phi -> x-y
Theta=[...
    +cos(phi(i+1)), -sin(phi(i+1));...
    +sin(phi(i+1)), +cos(phi(i+1))];

%% - Velocity in x-y
v=Theta*[vr(i+1);vphi(i+1)];
Xxy(i+1,4)=v(1,1);
Xxy(i+1,5)=v(2,1);

%% - Acceleration in x-y
a=Theta*[ar(i+1);aphi(i+1)];
Xxy(i+1,7)=a(1,1);
Xxy(i+1,8)=a(2,1);

end

%% Illustrations
figure;line('xdata',t(50:end),'ydata',r(50:end,1));title('r')
figure;line('xdata',t(50:end),'ydata',r(50:end,2));title('r dot')
figure;line('xdata',t(50:end),'ydata',r(50:end,3));title('r dot dot')
figure;line('xdata',t(50:end),'ydata',r(50:end,4));title('Dr dot dot')
figure;line('xdata',t(50:end),'ydata',vr(50:end,1));title('vr')
figure;line('xdata',r(1:50,1),'ydata',vr(1:50,1));title('Radial velocity'),xlabel('r (m)'),ylabel('vr (m/s)')
figure;line('xdata',t(50:end),'ydata',vphi(50:end,1));title('vphi')
figure;line('xdata',t(50:end),'ydata',ar(50:end,1));title('ar')
figure;line('xdata',t(50:end),'ydata',aphi(50:end,1));title('aphi')

figure,'g';line('xdata',Xxy(50:end,1),'ydata',Xxy(50:end,2),'LineWidth',2.5,'Color',[0 1 0]);title('x,y')
axis equal

```

```
axis([-0.345 +0.345 -0.345 +0.345])
grid on
```

```
%% Velocity & Aceleration
for i=(50:100:N)
x=Xxy(i+1,1);
y=Xxy(i+1,2);
z=Xxy(i+1,3);
u=Xxy(i+1,4)/10; %10 for scaling
v=Xxy(i+1,5)/10; %10 for scaling
w=Xxy(i+1,6);
d=Xxy(i+1,7)/500; %500 for scaling
e=Xxy(i+1,8)/500; %500 for scaling
f=Xxy(i+1,9);
ii_PlotVector(x,y,z,u,v,w)
ii_PlotVector(x,y,z,d,e,f)
cameratoolbar
end
```

6.3.4. Obtaining of the radial velocity and fitted models

- **Piecewise_Function_DEMO**

%Torben Brøchner & Paula Macías, 2014

```
function [ RadialVelocity ] = Piecewise_Function_DEMO(xLim,mH,nH,mB,nB,d,Dt)
```

```
xLim=xLim;
mH=mH;
nH=nH;
mB=mB;
nB=nB;
d=d;
Dt=Dt;
Inp1=1/2;
Inp2=0.9254; %Flow (kg/s)

nData=size(mH,2);
Constant=Dt;
DeltaX=Constant;
Idx=0;
for i=1:nData
    for x=xLim(i):DeltaX:xLim(i+1)
        y=mH(i)*x+nH(i);
        b=mB(i)*x+nB(i);
        A=y*b*Multiplier(Inp1);
        Idx=Idx+1;
        A_result(Idx)=A;
        z(i)=d(i);
        V_radial=Multiplier2(Inp2)./A_result;
    end
end

end
CrossSectionAreaArray=A_result;
RadialVelocity=V_radial;
```

```
function Mul=Multiplier(Inp1)
    Mul=Inp1;
end

function Mul2=Multiplier2(Inp2)
    Mul2=Inp2/z(i);
end

end
```

- **RadialVelocity_f_Area**

This code was designed to obtain the radial velocity based on the transversal area along the blade. This example is particularized for the 215rpm velocity.

%Torben Brøchner & Paula Macías, 2014

```
xLim=[0.040057 0.103338 0.107303 0.128255 0.129438 0.179671 0.200854 0.217406
0.246784 0.281];
mH=[0.5110 0.5110 -0.2058 -0.2058 0.2431 0.0458 0.0458 -0.4766 -0.4766];
nH=[-0.020468 -0.020468 0.056442 0.056442 -0.001666 0.033783 0.033783 0.147369
0.147369];
mB=[0.4003 -0.1173 -0.1173 -0.1173 -0.1173 -0.1173 -0.0227 -0.0227 -0.0227];
nB=[-0.016036 0.037461 0.037461 0.037461 0.037461 0.037461 0.018444 0.018444
0.018444];
d=[1732 1732 1732 1948.5 1948.5 1948.5 1515.5 1515.5 649.5]; % (kg/m3)

Dt=0.001;

RadialVelocity = Piecewise_Function_DEMO (xLim,mH,nH,mB,nB,d,Dt);

p1=xLim(1):Dt:xLim(2);
p2=xLim(2):Dt:xLim(3);
p3=xLim(3):Dt:xLim(4);
p4=xLim(4):Dt:xLim(5);
p5=xLim(5):Dt:xLim(6);
p6=xLim(6):Dt:xLim(7);
p7=xLim(7):Dt:xLim(8);
p8=xLim(8):Dt:xLim(9);
p9=xLim(9):Dt:xLim(10);
p=[p1 p2 p3 p4 p5 p6 p7 p8 p9];
grid on
plot(p(20:end),RadialVelocity(20:end),'k','linewidth',2)
grid on
```

6.3.5. Modeling of rotating spreader disk with straight blades

This code was written to create a patch object, a spreader disk, by defining its vertices, faces and colours. Movement was also incorporated.

- **Movement around z axis**

```
function R = Rotation(W)
    w1 = W(1);
    w2 = W(2);
    w3 = W(3);
```

```
R1 = [1, 0, 0;
      0, cos(w1), -sin(w1);
      0, sin(w1), cos(w1)];

R2 = [cos(w2), 0, sin(w2);
      0, 1, 0;
      -sin(w2), 0, cos(w2)];

R3 = [cos(w3), -sin(w3), 0;
      sin(w3), cos(w3), 0;
      0, 0, 1];

R = R1*R2*R3;
```

- **Vertices**

```
function VertexData =
Vertices(Location,Orientation,SideLength,Blades,Diameter,Height,Distance,Division)
r = Location;
R = Orientation;
Lx = SideLength(1);
Ly = SideLength(2);
Lz = SideLength(3);
n = Blades;
dia = Diameter;
h = Height;
D = Distance;
a = Division;

%Pre-needed calculations
tita=360/n;
ra=dia/2;

%Generate vertices blades
V=zeros(n*8,3);
for i=1:n; V(1+8*(i-1),1:3)=[-D*sind(i*tita)+(-Lz/2)*cosd(i*tita),D*cosd(i*tita)+(-
Lz/2)*sind(i*tita),0]; end
for i=1:n; V(2+8*(i-1),1:3)=[-D*sind(i*tita)+(-Lz/2)*cosd(i*tita),D*cosd(i*tita)+(-
Lz/2)*sind(i*tita),Ly]; end
for i=1:n; V(3+8*(i-1),1:3)=[-
D*sind(i*tita)+(Lz/2)*cosd(i*tita),D*cosd(i*tita)+(Lz/2)*sind(i*tita),Ly]; end
for i=1:n; V(4+8*(i-1),1:3)=[-
D*sind(i*tita)+(Lz/2)*cosd(i*tita),D*cosd(i*tita)+(Lz/2)*sind(i*tita),0]; end
for i=1:n; V(5+8*(i-1),1:3)=[-(Lx+D)*sind(i*tita)-(Lz/2)*cosd(i*tita),(Lx+D)*cosd(i*tita)+(-
Lz/2)*sind(i*tita),0]; end
for i=1:n; V(6+8*(i-1),1:3)=[-(Lx+D)*sind(i*tita)-(Lz/2)*cosd(i*tita),(Lx+D)*cosd(i*tita)+(-
Lz/2)*sind(i*tita),Ly]; end
for i=1:n; V(7+8*(i-1),1:3)=[-
(Lx+D)*sind(i*tita)+(Lz/2)*cosd(i*tita),(Lx+D)*cosd(i*tita)+(Lz/2)*sind(i*tita),Ly]; end
for i=1:n; V(8+8*(i-1),1:3)=[-
(Lx+D)*sind(i*tita)+(Lz/2)*cosd(i*tita),(Lx+D)*cosd(i*tita)+(Lz/2)*sind(i*tita),0]; end
X_blade = V;

%Generate vertices disk
G=zeros((360/a)*6,3);
for i=1:360/a; G(1+(i-1)*6,1:3)=[0,0,-h]; end
for i=1:360/a; G(2+(i-1)*6,1:3)=[ra*sind((i+1)*a),ra*cosd((i+1)*a),-h]; end
for i=1:360/a; G(3+(i-1)*6,1:3)=[ra*sind(i*a),ra*cosd(i*a),-h]; end
```

```

for i=1:360/a; G(4+(i-1)*6,1:3)=[0,0, 0]; end
for i=1:360/a; G(5+(i-1)*6,1:3)=[ra*sind((i+1)*a),ra*cosd((i+1)*a), 0]; end
for i=1:360/a; G(6+(i-1)*6,1:3)=[ra*sind(i*a),ra*cosd(i*a), 0]; end
X_disk = G;

```

```
VertexData_0 = [V;G];
```

```
n_ver = n*8+(360/a)*6;
```

```

for i_ver=1:n_ver
    VertexData(i_ver,:) = r + VertexData_0(i_ver,:)*R';

```

```
end
```

- **Faces**

```

function [PatchData_X,PatchData_Y,PatchData_Z] = Faces(VertexData,Blades,Division)
a = Division;
n = Blades;

```

```
%Generate triangular faces
```

```

F=zeros(n*12,3);
for i=1:n; F(1+(i-1)*12,1:3)=[1+(i-1)*8, 2+(i-1)*8, 3+(i-1)*8]; end
for i=1:n; F(2+(i-1)*12,1:3)=[1+(i-1)*8, 3+(i-1)*8, 4+(i-1)*8]; end
for i=1:n; F(3+(i-1)*12,1:3)=[1+(i-1)*8, 2+(i-1)*8, 6+(i-1)*8]; end
for i=1:n; F(4+(i-1)*12,1:3)=[1+(i-1)*8, 6+(i-1)*8, 5+(i-1)*8]; end
for i=1:n; F(5+(i-1)*12,1:3)=[5+(i-1)*8, 6+(i-1)*8, 7+(i-1)*8]; end
for i=1:n; F(6+(i-1)*12,1:3)=[5+(i-1)*8, 7+(i-1)*8, 8+(i-1)*8]; end
for i=1:n; F(7+(i-1)*12,1:3)=[1+(i-1)*8, 4+(i-1)*8, 8+(i-1)*8]; end
for i=1:n; F(8+(i-1)*12,1:3)=[1+(i-1)*8, 8+(i-1)*8, 5+(i-1)*8]; end
for i=1:n; F(9+(i-1)*12,1:3)=[4+(i-1)*8, 3+(i-1)*8, 7+(i-1)*8]; end
for i=1:n; F(10+(i-1)*12,1:3)=[4+(i-1)*8, 7+(i-1)*8, 8+(i-1)*8]; end
for i=1:n; F(11+(i-1)*12,1:3)=[2+(i-1)*8, 6+(i-1)*8, 3+(i-1)*8]; end
for i=1:n; F(12+(i-1)*12,1:3)=[3+(i-1)*8, 6+(i-1)*8, 7+(i-1)*8]; end
C_blade = F;

```

```
%Generate triangular faces
```

```

H=zeros((360/a)*4,3);
for i=1:360/a; H(1+(i-1)*4,1:3)=[(1+(i-1)*6)+n*8, (2+(i-1)*6)+n*8, (3+(i-1)*6)+n*8]; end
for i=1:360/a; H(2+(i-1)*4,1:3)=[(4+(i-1)*6)+n*8, (5+(i-1)*6)+n*8, (6+(i-1)*6)+n*8]; end
for i=1:360/a; H(3+(i-1)*4,1:3)=[(2+(i-1)*6)+n*8, (5+(i-1)*6)+n*8, (3+(i-1)*6)+n*8]; end
for i=1:360/a; H(4+(i-1)*4,1:3)=[(5+(i-1)*6)+n*8, (3+(i-1)*6)+n*8, (6+(i-1)*6)+n*8]; end
C_disk = H;

```

```
Index_Patch = [F;H];
```

```
n_pat = n*12+(360/a)*4;
```

```

for i_pat=1:n_pat
    PatchData_X(:,i_pat) = VertexData(Index_Patch(i_pat,:),1);
    PatchData_Y(:,i_pat) = VertexData(Index_Patch(i_pat,:),2);
    PatchData_Z(:,i_pat) = VertexData(Index_Patch(i_pat,:),3);
end

```

- **DiskCreationUnderMovement**

```

%% Blade data
Lx = 28.1;
Ly = 5;
Lz = 0.3;
n = 3; %number of blades
D = 8; %distance between centre and blade's edge

%% Disk data
dia = 50; %disk diameter
h = 1; %disk height
a = 10; %division angle

%% Motion data
t = [0:0.005:2]'; % Time data
r = [0*t, 0*t, 0*t]'; % Position data
W = [0*t, 0*t, 12*pi*t]'; % Orientation data (x-y-z)

%%Pre-needed calculations
tita=360/n;
ra=dia/2;
n_time = length(t);

% Compute propagation of vertices and patches
for i_time=1:n_time
    R = Rotation(W(i_time,:));
    VertexData(:,i_time) = Vertices(r(i_time,:),R,[Lx,Ly,Lz],n,dia,h,D,a);
    [X,Y,Z] = Faces(VertexData(:,i_time),n,a);
    PatchData_X(:,i_time) = X;
    PatchData_Y(:,i_time) = Y;
    PatchData_Z(:,i_time) = Z;
    PatchData_C(:,i_time) = [0.6, 0.6, 0.6];
end

% Draw figure
figure(1);
h = patch(PatchData_X(:,1),PatchData_Y(:,1),PatchData_Z(:,1),PatchData_C(:,1));
set(h,'FaceLighting','phong','EdgeLighting','phong','edgcolor','none');
set(h,'EraseMode','normal');

% Axes settings
xlabel('x','FontSize',14);
ylabel('y','FontSize',14);
zlabel('z','FontSize',14);
set(gca,'FontSize',14);
axis vis3d equal;
view([0,0]);
camlight;
grid on;
xlim([-70,70]);
ylim([-70,70]);
zlim([-70,70]);

% Animation Loop
for i_time=1:n_time
    set(h,'XData',PatchData_X(:,i_time));
    set(h,'YData',PatchData_Y(:,i_time));
    set(h,'ZData',PatchData_Z(:,i_time));

```

```
set(h,'CData',PatchData_C(:,:,i_time));  
drawnow;  
end  
  
%Prepare the new file.  
writerObj = VideoWriter('disk.avi');  
open(writerObj);  
  
%Generate initial data and set axes and figure properties.  
set(gca,'nextplot','replacechildren');  
set(gcf,'Renderer','zbuffer');  
  
%Create a set of frames and write each frame to the file.  
for i_time = 1:100  
    set(h,'XData',PatchData_X(:,:,i_time));  
    set(h,'YData',PatchData_Y(:,:,i_time));  
    set(h,'ZData',PatchData_Z(:,:,i_time));  
    set(h,'CData',PatchData_C(:,:,i_time));  
    frame = getframe;  
    writeVideo(writerObj,frame);  
end  
  
close(writerObj);
```